Available online at www.sciencedirect.com
SCIENCE DIRECT®
Coastal Engineering 51 (2004) 53–80
Coastal Engineering
An International Journal for Coastal, Harbour and Offshore Engineers
www.elsevier.com/locate/coastaleng

Numerical simulation of breaking waves by a multi-scale turbulence model

Qun Zhao[a,*], Steve Armfield[b], Katsutoshi Tanimoto[c]

[a] Center for Applied Coastal Research, University of Delaware, Newark, DE 19716, USA
[b] Department of Mechanical Engineering, Sydney University, Sydney 2006, Australia
[c] Department of Civil Engineering, Saitama University, Urawa, Saitama 338-8570, Japan

Received 24 June 2002; received in revised form 15 December 2003; accepted 15 December 2003

Abstract

In this paper, a two-dimensional multi-scale turbulence model is proposed to study breaking waves. The purpose of developing this model is to produce a relatively accurate model with moderate computer requirements. The free surface is tracked by the VOF technique, the log-law profile for the mean velocity is applied at the bottom. Comparing with the Reynolds-Averaged Navier-Stokes models (RANS), the present model shows improving agreement with experimental measurements in terms of surface elevations, particle velocities, wave height distributions and undertow profiles. The subgrid scale (SGS) turbulent transport mechanism is also discussed in the paper. It is found that turbulent production and dissipation are of the same order, but turbulent production is primarily located at the wavefront and above the wave trough, whereas turbulent dissipation is primarily located at the back face of a wave, indicating that in these regions, the assumption of equilibrium is not correct. Below the trough level, the local equilibrium assumption is reasonable. Turbulent convection and diffusion are of the same order at the trough level. Above the trough level, turbulent convection dominates. Under the spilling breaking wave, turbulent kinetic energy is continue to dissipate in the bore region, whereas under the plunging breaking wave, the turbulent kinetic energy is dissipated very rapidly within one wave period.

Keywords: Multi-scale turbulence model; VOF method; Breaking wave; Turbulent kinetic energy cascade; Reynolds-averaged Navier–Strokes (RANS) model

1. Introduction

The present stage of Navier-Stokes equations based numerical modeling (MAC or VOF) of breaking waves in coastal and ocean engineering can be classified into three levels: (I) those that solve the Navier-Stokes equations directly, containing no turbulence models (Miyata, 1986), or include constant eddy viscosity in both space and time (Petit et al., 1994); (II) those that solve the Reynolds-Averaged Navier-Stokes (RANS) equations (Lemos, 1992; Lin and Liu, 1998a,b; Bradford, 2000; Christensen et al., 2000); (III) and those that solve the space-filtered Navier-Stokes equations (Zhao and Tanimoto, 1998; Wijayaratna and Okayasu, 2000; Christensen and Deigaard, 2001).

A very early attempt at solving breaking waves by the Navier-Stokes equations is that of Miyata (1986).

* Corresponding author.
E-mail address: zhao@coastal.udel.edu (Q. Zhao).

0378-3839/$ - see front matter © 2004 Elsevier B.V. All rights reserved.
doi:10.1016/j.coastaleng.2003.12.002

In that paper, breaking waves on an isolated obstacle were simulated by a two-dimensional MAC type finite difference method. The third-order upwind scheme proposed by Kawamura and Kawahara (1984) was applied to discretize the convective terms. Based on the argument of Kawamura and Kawahara (1984) that the fourth-derivative error plays the role of a turbulence model, Miyata (1986) employed no turbulence model in his simulation. Comparisons between the computed and measured surface profiles showed fairly good agreement. On the other hand, Petit et al. (1994) applied a constant eddy viscosity, roughly 1000 times the kinematic viscosity, in both space and time, to simulate the energy cascade and maintain the smoothness of the solution. Considering the errors due to the definition of incoming waves at the inflow boundary (Petit et al., 1994), their model showed reasonable agreement with experimental measurements. Although the above exercises are not totally unrealistic, these procedures may adversely affect a somewhat wider band of the turbulence spectrum than a purpose-designed turbulence model.

The second class of numerical models are those based on Reynolds-Averaged Navier-Stokes (RANS) equations. Lemos (1992) first applied the standard k–ε model to simulate breaking waves on coastal structures. Only qualitative results are presented in that paper. Lin and Liu (1998a,b) carried out a detailed investigation and evaluation of breaking wave kinematics and turbulence in the surf zone. Their results showed that the algebra Reynolds stress model can provide very good results at the shoaling region and in the inner surf zone. Near the breaking point, however, the Reynolds stress model always overestimates the eddy viscosity, which leads to excessive mixing, and thus underestimates surface elevations. A very good review and comparisons among popular k–ε class models has been presented recently by Bradford (2000). In that paper, Bradford compared the performance of the k model, linear k–ε model and a Renormalized Group extension of the k–ε model (RNG model). Comparing with the same sets of data (Ting and Kirby 1994, 1995, 1996) as Lin and Liu (1998a,b), all the k–ε class models in Bradford (2000) showed the same trend as that of the Reynolds stress model for the spilling breaker (Lin and Liu, 1998a): the k–ε class models give generally good results in the shoaling zone and in the inner surf zone, but they predict the wave breaking far earlier than that observed in experiment (the breaking point x_b is at 4.73 m in the numerical simulation, but 6.4 m in the physical experiment), while also underestimating the undertows. However, the general agreement of wave heights, surface elevations and undertows with experiments for the plunging breaker case with the Reynolds stress model and RNG models (Bradford, 2000) is better than that for a spilling breaker. More recently, Christensen et al. (2000) applied a k–ω model to simulate the same set of data (Ting and Kirby 1994, 1995, 1996), and showed that their model significantly underestimate the undertow profiles for the spilling breaker case but overpredict for the plunging breaker case. However, in the inner surf zone of the plunging breaker, the k–ω model provides much better undertow profile. In our opinion, the reason maybe that for the plunging breaker, the vertical mixing is stronger and the energy spectrum is closer to the equilibrium range, as assumed in the standard k–ε class model, than that of the spilling breaker.

The third class of numerical models are based on space-filtered Navier-Stokes equations. Zhao and Tanimoto (1998) applied a cell volume filter to the Navier-Stokes equations with the filtered Navier-Stokes equations then solved in two dimensions. In that exercise, the Smagorinsky model was used to model the subgrid scale turbulence. Their model cannot provide three-dimensional vortex stretching, however, due to the dissipative nature of the Smagorinsky model, two-dimensional vortex stretching was enabled via the artificial viscosity. In that sense, the Smagorinsky model behaves like a mixing length turbulence model, with the turbulence length scale equal to the Smagorinsky length scale. The modeled surface elevations and wave heights were compared with experimental measurements and showed good agreement. Recently, Christensen and Deigaard (2001) presented three-dimensional LES, and Wijayaratna and Okayasu (2000) DNS, of breaking waves, respectively. All of these studies showed remarkable impressions of breaking waves, however, the computations were very time consuming. Still the calculation of Wijayaratna and Okayasu (2000) was performed only for one wavelength. Besides, there is no model-data comparison has been made.

Instead, in the present paper, a two-dimensional, multi-scale, non-equilibrium subgrid scale turbulence

model is proposed that can be applied to coastal engineering problems. Unlike those models in classes II and III, the present model will fully resolve the large-scale two-dimensional flow structures while modeling the three-dimensional turbulence interactions.

In this paper, we first present the physical and mathematical framework for the model, and then compare the numerical results with the experimental measurements as well as the numerical results of the Reynolds stress model (Lin and Liu, 1998a,b) and RNG group model (Bradford, 2000). Finally, discussions of SGS turbulent transport mechanisms will also be presented.

2. Governing equations

The numerical model used here is based on the VOF method, which was developed by Hirt and Nichols (1981) and then further modified by Zhao and Tanimoto (1998) to be suitable for the computation of wave problems. The governing equations are the continuity equation for incompressible flow

$$\frac{\partial u_j}{\partial x_j} = 0 \tag{1}$$

and the Navier-Stokes equation in the x–z plane,

$$\frac{\partial u_i}{\partial t} + u_j \frac{\partial u_i}{\partial x_j} = -\frac{1}{\rho}\frac{\partial p}{\partial x_i} + \nu \frac{\partial^2 u_i}{\partial x_j \partial x_j} + g_i, \tag{2}$$

where $i=1$, 3 are indices in the x and z direction, respectively, and j is a repeated dummy index, ν is the kinematic viscosity and g_i the gravitational acceleration, where $g_1=0$, p is the pressure, and ρ the fluid density with t the time.

In order to describe the free water surface, the VOF method introduces a volume of fluid function $F(x, z, t)$ to define the fluid region. The physical meaning of the F function is the fractional volume of the cell occupied by the fluid. A unit value of F corresponds to a cell full of fluid, while a zero value indicates that the cell contains no fluid. Cells with F values between zero and one must then contain a free surface. The time dependence of F is governed by the equation,

$$\frac{\partial F}{\partial t} + u_j \frac{\partial F}{\partial x_j} = 0. \tag{3}$$

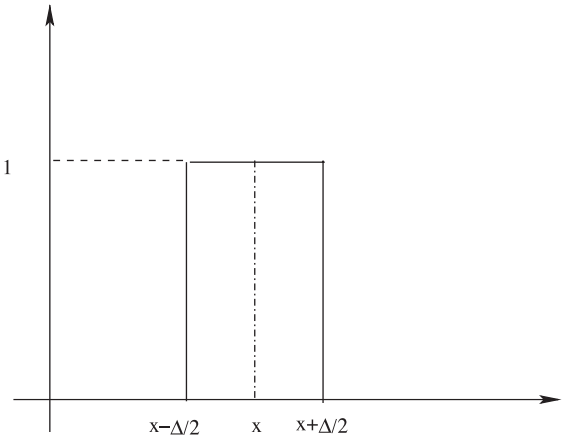

Fig. 1. The top-hat filter.

However, the instantaneous Eqs. (1)–(3) cannot be used to solve the wave breaking problem directly due to strong turbulence that occurs, and the limitation of the grid size in a numerical simulation. An approximation of the turbulent flow, a turbulence closure model, is needed to close the system of the equations.

There are several choices for the different levels of approximations as well as associated turbulence models. In the present work, we will use a space filter, i.e., the top-hat filter, to filter Eqs. (1)–(3). The top-hat filter is defined as, see Fig. 1 for a one-dimensional example,

$$G(x-\xi) = \begin{cases} 1 & \text{if } |x-\xi| \le \dfrac{\Delta}{2} \\ 0 & \text{otherwise} \end{cases} \tag{4}$$

here Δ is the typical length scale.

Then the filtered continuity and Navier-Stokes equations read (Deardorff, 1970),

$$\frac{\partial \bar{u}_j}{\partial x_j} = 0, \tag{5}$$

$$\frac{\partial \bar{u}_i}{\partial t} + \bar{u}_j \frac{\partial \bar{u}_i}{\partial x_j} = -\frac{1}{\rho}\frac{\partial \bar{p}}{\partial x_i} + \nu \frac{\partial^2 \bar{u}_i}{\partial x_j \partial x_j} - \frac{\partial}{\partial x_j}\left(\overline{u_i u_j} - \bar{u}_i \bar{u}_j\right) + g_i, \tag{6}$$

where the overbar denotes the filtered (resolvable) quantities. For example, the filtered particle velocity is

$$\bar{u}_i(x,z,t) = \frac{1}{\Delta x \Delta z}\int_{x-\frac{1}{2}\Delta x}^{x+\frac{1}{2}\Delta x}\int_{z-\frac{1}{2}\Delta z}^{z+\frac{1}{2}\Delta z} u_i(\zeta,\eta,t)\mathrm{d}\zeta\mathrm{d}\eta \tag{7}$$

in which Δx and Δz are the grid size of the finite difference equation in the x and z directions, respectively. Also, $\bar{u}_i$ are the filtered particle velocity components, $\bar{p}$ is the filtered pressure. The new term appearing in the filtered equations is:

$$R_{ij} = \overline{u_i u_j} - \bar{u}_i \bar{u}_j \tag{8}$$

where R_{ij} is called the subgrid scale (SGS) Reynolds stress. It is noticed that R_{ij} is similar to the RANS Reynolds stress, but the physics it represents is different. In RANS models, all the turbulence motions are modeled, while in LES models, only the turbulence motions smaller than the filter size (subgrid scale) are modeled, the turbulence motions larger than the filter size (“large eddies”) are explicitly computed. The large scale motions are affected by the flow geometry and are different from flow to flow, while the small scale motions are more universal. Therefore, it is reasonable to expect that the model closure for LES is less demanding than that by RANS models, and thus, LES models are expected to be more accurate and reliable than RANS models, especially for flows in which large-scale unsteadiness is significant.

Using the Boussinesq assumption, the SGS Reynolds stress is approximated as

$$R_{ij} = -2\nu_T S_{ij}, \tag{9}$$

where ν_T is the SGS eddy viscosity, and S_{ij} is the shear strain rate tensor for the resolved scales.

$$S_{ij} = \frac{1}{2}\left(\frac{\partial \bar{u}_i}{\partial x_j} + \frac{\partial \bar{u}_j}{\partial x_i}\right). \tag{10}$$

Substituting the above equations into Eq. (6), we get the final form for the space filtered Navier-Stokes equations,

$$\frac{\partial \bar{u}_i}{\partial t} + \bar{u}_j \frac{\partial \bar{u}_i}{\partial x_j} = -\frac{1}{\rho}\frac{\partial \bar{p}}{\partial x_i} + \frac{\partial}{\partial x_j}\left[(\nu + \nu_T)\frac{\partial \bar{u}_i}{\partial x_j}\right] + g_i. \tag{11}$$

Now we need a turbulence closure to model the unresolved scale (SGS) motions.

3. The multi-scale turbulence model

As noted in Section 1, three-dimensional LES or DNS are still too computationally expensive to use in practice for the breaking wave problem, when the resulting Reynolds number is too high. Here, we propose a two-dimensional model that is both accurate and computationally efficient.

The problem with existing two-dimensional LES models is that for the ideal case (no numerical dissipation), it has been derived and proved that there is a reverse energy cascade (Kraichnan, 1967; Lilly, 1969, etc.) in the 2D model, i.e., the turbulent kinetic energy is transferred to larger scales. This reverse energy cascade is unphysical and means that conventional LES models should be used in 3D form only.

An alternative to the use of direct numerical simulation is to use the RANS equations. However, as shown in the previous section, the agreement between the calculations and the experimental measurements are not promising near the breaking point for RANS models. This is likely due to the fact that single scale RANS models assume that one length scale can represent the entire range of eddy sizes in a turbulent flow, and therefore, the length scale of the energy-containing (large) eddies is universally proportional to the length scale of the energy-dissipation (smallest) eddies. However, for flows where the energy spectrum is not in equilibrium, the different sizes of turbulent eddies show different rates of development therefore need to be modeled separately with appropriate modeling of interactions. The improved model accuracy in the plunging breaker case of Lin and Liu (1998b) and Bradford (2000) also suggest that due to the strong mixing in the plunging breaker, the flow is closer to a spectral equilibrium where the single-scale hypothesis could be adequate.

Inspired by the multiple-time-scale concept proposed by Hanjalic et al. (1980) and the encouraging results to various applications (Hanjalic et al., 1980; Kim, 1991; Guo and Rhode, 1996, etc.), we propose a multi-scale k–l model, in which a compromise of the RANS and 3D LES approaches is achieved by setting up an artificial energy cascade process explicitly using a multi-scale subgrid approach that allows energy transfers between scales. Fig. 2 shows a sketch of this idea. In Fig. 2, we have parameterized the unresolved turbulence motions into several length scales starting from the smallest resolved length scale κ_1, where κ is the wave number, to a cut-off length

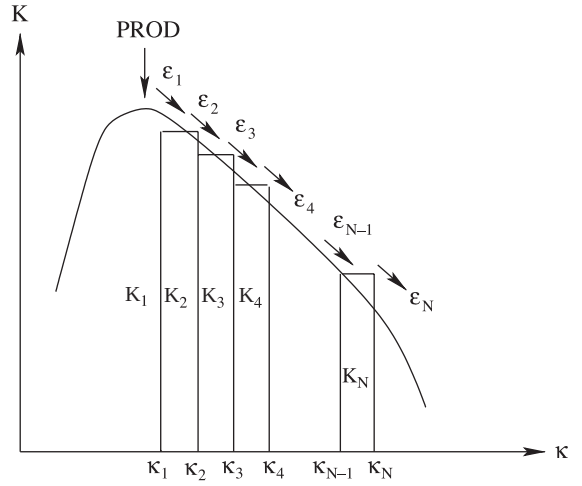

Fig. 2. Partition of the spectra density.

scale κ_N of the simulation, with each length scale $l_n = l_g / 2^{(n-1)}$ and l_g the grid scale, $\sqrt{\Delta x \Delta z}$. The cut-off length scale is chosen to fall inside the inertial subrange, and thus can be assumed to be in local equilibrium where a simple subgrid model can be applied.

We set up N levels of k–l equations, in which turbulent kinetic energy can be transferred from larger length scales to smaller ones explicitly (see Fig. 2). In this approach, the production term at the first level is dominated by the "large eddies", i.e., the smallest resolved scale (the grid scale, in this case),

$$\mathrm{PROD}_1 = \nu_{t_1}\left[\frac{1}{2}\left(\frac{\partial \bar{u}_i}{\partial x_j}+\frac{\partial \bar{u}_j}{\partial x_i}\right)\left(\frac{\partial \bar{u}_i}{\partial x_j}+\frac{\partial \bar{u}_j}{\partial x_i}\right)\right], \quad (12)$$

The dissipation term is the k–l type dissipation,

$$\epsilon_n = C_d k_n^{\frac{3}{2}}/l_n, \qquad 1 \le n < N, \quad (13)$$

where the length scale for each partition is

$$l_n = \frac{\sqrt{\Delta x \Delta z}}{2^{n-1}} \qquad 1 \le n < N \quad (14)$$

Within each partition $n>1$, production is set equal to dissipation at the next n-level grid scale partition,

$$\mathrm{PROD}_n = \varepsilon_{n-1} \qquad 2 \le n \le N. \quad (15)$$

Then the total SGS turbulent kinetic energy is the sum of the kinetic energy in all partitions,

$$k = k_1 + k_2 + \ldots + k_N = \sum_{n=1}^{N} k_n. \quad (16)$$

We also assume that turbulent kinetic energy leaves the system at the smallest scales, therefore, the total dissipation of the system is characterized as

$$\epsilon = \epsilon_N. \quad (17)$$

The eddy viscosity ν_{t_n} at the n level is thus set to all the scales smaller than n,

$$\nu_{t_n} = \sum_{i=n}^{N} C_s k_i^{\frac{1}{2}} l_i \quad 1 \le n < N. \quad (18)$$

Then the nth level k–l equation reads,

$$\frac{\partial k_n}{\partial t} + u_j \frac{\partial k_n}{\partial x_j} = \frac{\partial}{\partial x_j}\left(\frac{\nu_{t_n}}{\sigma_k}\frac{\partial k_m}{\partial x_j}\right) + \mathrm{PROD}_n - \epsilon_n. \quad (19)$$

For the results shown in this paper, $C_d = 0.17$, $C_s = 0.1$ and $\sigma_k = 1.0$ are used. However, sensitivity tests have been conducted with $C_d = 0.17$–0.2, $C_s = 0.1$–0.2, and within these ranges, the numerical results were found to be insensitive to the model values.

Finally, the space filtered Navier-Stokes equations read,

$$\frac{\partial \bar{u}_i}{\partial t} + \bar{u}_j \frac{\partial \bar{u}_i}{\partial x_j} = -\frac{1}{\rho}\frac{\partial \bar{p}}{\partial x_i} + \frac{\partial}{\partial x_j}\left[(\nu + \nu_T)\frac{\partial \bar{u}_i}{\partial x_j}\right] + g_i. \quad (20)$$

$$\nu_T = \nu_{t_1}, \quad (21)$$

in which ν_{t_1} is the eddy viscosity for all the length scales smaller than the smallest resolved scales.

Eqs. (12)–(19) show that in the multi-scale turbulence model, eddies with different length scales are recognized and treated differently with proper interactions. The single scale turbulence models, on the other hand, do not recognize the differences among the dissipation rates, i.e., they assume $\epsilon_1 = \epsilon_2 = \ldots = \epsilon_N$, which is only true when the flow reaches equilibrium stage.

4. Numerical method

Following Hirt and Nichols (1981), the computational solutions of the above equations are obtained on a staggered grid. Fig. 3 shows the locations of the velocity components, pressure, F function, as well as the SGS turbulent kinetic energy $k^n_{i,J}$ and eddy viscosity $v^n_{ti,j}$. The pressure $p_{i,j}$, volume of fluid function $F_{i,j}$, SGS turbulent kinetic energy $k^n_{i,j}$ and eddy viscosity $v^n_{ti,j}$ are cell-centered quantities, while the velocity components are defined at the cell faces. Δx_i and Δz_j are the mesh sizes at ith column and jth row.

Then the discrete form of the momentum equations read,

$$u^{m+1}_{i+\frac{1}{2},j} = Q_{i+\frac{1}{2},j} - \frac{\Delta t}{\Delta x_{i+\frac{1}{2}}}\left(p^{m+1}_{i+1,j} - p^{m+1}_{i,j}\right), \tag{22}$$

$$w^{m+1}_{i,j+\frac{1}{2}} = R_{i,j+\frac{1}{2}} - \frac{\Delta t}{\Delta z_{j+\frac{1}{2}}}\left(p^{m+1}_{i,j+1} - p^{m+1}_{i,j}\right), \tag{23}$$

$$Q_{i+\frac{1}{2},j} = u_{i+\frac{1}{2},j} + \Delta t[-\mathrm{FUX} - \mathrm{FUZ} + \mathrm{VISX}], \tag{24}$$

$$R_{i,j+\frac{1}{2}} = w_{i,j+\frac{1}{2}} + \Delta t[-\mathrm{FWX} - \mathrm{FWZ} + \mathrm{VISZ}], \tag{25}$$

in which the superscript $m+1$ denotes the variables at the new time level, while variables without superscript are taken at the old time level, m. The first order forward Euler scheme is used here as in Lin and Liu (1998a,b), and Bradford (2000), because higher order in time schemes are generally difficult to apply for the F function.

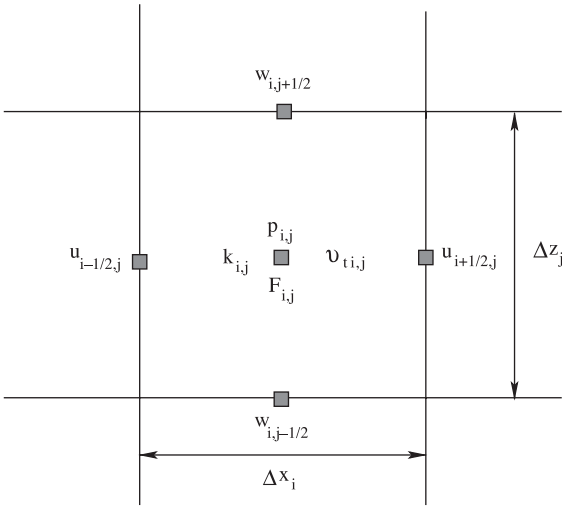

Fig. 3. Stagger grid and locations of variables.

The FUX, FUZ and FWX, FWZ are the convective terms in the x and z directions in the u and w momentum equations, respectively, and VISX and VISZ are the viscous diffusion terms. For example, in the u momentum equation, they are

$$\mathrm{FUX} = \left(u\frac{\partial u}{\partial x}\right)_{i+\frac{1}{2},j}, \tag{26}$$

$$\mathrm{FUZ} = \left(u\frac{\partial w}{\partial z}\right)_{i+\frac{1}{2},j}, \tag{27}$$

$$\mathrm{VISX} = \frac{\partial}{\partial x}\left[(v+v_T)\frac{\partial \bar{u}}{\partial x}\right] + \frac{\partial}{\partial z}\left[(v+v_T)\frac{\partial \bar{u}}{\partial z}\right], \tag{28}$$

In the above, the convective terms are discretized using a fourth-order centered scheme, while the diffusion terms are discretized using a second-order centered scheme. All the variables have been discretized at location $(i+1/2,\ j)$ in the u momentum equation, and $(i, j+1/2)$ in the w momentum equation.

Because the pressure at time $m+1$ level is not known at the beginning of each time cycle, Eqs. (22) and (23) cannot be used directly to evaluate u^{m+1} and w^{m+1}, but must be combined with the continuity equation. In the first step of the solution, the p^{m+1} values are replaced by p^m to get a first guess for the new velocities.

The discrete form of the continuity equation is

$$\left(u^{m+1}_{i+\frac{1}{2},j} - u^{m+1}_{i-\frac{1}{2},j}\right)\Big/\Delta x_i + \left(w^{m+1}_{i,j+\frac{1}{2}} - w^{m+1}_{i,j-\frac{1}{2}}\right)\Big/\Delta z_j = 0. \tag{29}$$

Substituting Eqs. (22) and (23) into Eq. (29), we obtain the Poisson equation for the pressure with the source term expressed by Q and R at the m time level. The Poisson equation is solved using the SOR method.

The volume of fluid function F is advanced after the velocity and pressure fields are obtained. Combining with the continuity Eq. (5), the filtered volume of fluid equation can be written in a conservation form

$$\frac{\partial F}{\partial t} + \frac{\partial F\bar{u}_j}{\partial x_j} = 0. \tag{30}$$

According to the definition, we know that F is a step function, therefore, the standard finite-difference approximations will lead to smearing of the F function, and interfaces will lose their definition. In the VOF method, a donor–acceptor method is introduced to compute the F function (Hirt and Nichols, 1981).

In order to prevent the numerical instability or inaccuracy, appropriate mesh increments Δx_i, Δz_j and time increment Δt should be selected. For accuracy, the mesh increments must be chosen small enough to resolve the expected spatial variations in all dependent variables.

Once a mesh has been chosen, the choice of the time increment for stability is governed by two restrictions. First, the CFL condition states that material should not move through more than one cell in one time step, because the difference equations assume the fluxes transport quantities only between adjacent cells. Therefore, the time increment must satisfy the inequality,

$$\Delta t \leq \min\left\{\frac{\Delta x_i}{|u_{i,j}|}, \frac{\Delta z_j}{|w_{i,j}|}\right\}, \tag{31}$$

where the minimum is with respect to every cell in the mesh. Normally, Δt is chosen one-fourth to one-third of the minimum cell transit time. Second, when a nonzero value of viscosity is used, momentum must not diffuse more than approximately one cell in one time step. This limitation implies

$$(\nu + \nu_T)\Delta t \leq \frac{1}{2}\frac{\Delta x_i^2 \Delta z_j^2}{\Delta x_i^2 + \Delta z_j^2}. \tag{32}$$

In the program, Δt is automatically adjusted for each time step to obtain maximum efficiency.

The wave problem governed by Eqs. (1)–(3) forms an initial-boundary value problem, the initial and boundary conditions need to be prescribed correctly.

Offshore, the incident waves are sent to the computation domain by prescribing the water surface elevation and particle velocities at the inflow boundary. An absorbing-generating wave-maker that simulates a piston-type wavemaker is also available (Zhao, 1998). This is used when a reflective structure is in the numerical wave channel (Zhao and Tanimoto, 1998). To lower the effect of initial surge in the numerical simulation, the surface elevation, horizontal velocities and pressures of the incident waves are given in forms such that at the start of the numerical simulation, the variables are naturally zero (or near to zero). Moreover, we have also applied a ramping function to the incident wave height, so that the incident waves will ramp up to the design wave height slowly. These measures will reduce the initial surge in the numerical wave flume significantly.

The VOF method with partial cell treatment (Torrey et al., 1985) can handle wave run up on a sloping bottom naturally, provided the grid sizes are sufficiently small (Lin and Liu, 1999). Our experience showed that the wall boundary condition needs to be implemented to obtain accurate undertow profiles. Here, the wall boundary condition described by Rodi (1980) is used. For a problem with open boundary, the boundary condition with a damping zone (Arai et al., 1993) is utilized.

Then the basic procedure for advancing a solution through one time increment Δt consists of four steps: (1) Explicit approximations of momentum equations are used to compute the first guess for new time level velocities using initial conditions or the previous time level values for all advective, pressure, and viscous accelerations. (2) To satisfy the continuity equation, pressures are iteratively adjusted in each cell and velocity changes induced by each pressure changes are added to the velocities computed in step (1). (3) The F function defining fluid regions must be updated to give the new fluid configuration. (4) Finally, the k–l equations are solved using the new velocities and the eddy viscosity for the new time step is obtained. Repetition of these steps will advance a solution through any desired time interval.

5. Model performance

Numerical simulations of breaking waves on a sloping beach are conducted to evaluate the performance of the present model. To facilitate comparisons with other models, we use the same set of data (Ting and Kirby, 1994, 1995, 1996) as that used by Lin and Liu (1998a,b) and Bradford (2000) for spilling and plunging breakers. Besides the experimental data, we also compared our model results with those of a Reynolds stress model (Lin and Liu, 1998a,b) and a RNG model (Bradford, 2000). How-

ever, it is noticed that Lin and Liu (1998a,b) did not present wave height distribution and undertow profiles while Bradford (2000) did not present the surface elevations.

In the laboratory experiment, cnoidal waves are generated in a water depth of 0.4 m by a bulkhead wave generator. Details of the experimental set-up may be found in the work of Ting and Kirby (1994). Fig. 4 shows a sketch of the experimental setup and the coordinate system.

In the numerical simulation, cnoidal waves are generated at the inflow boundary using the 3rd order theory presented by Horikawa (1988). The computation starts at $x = -5.0$ m from the toe of the slope. The calculation domain is 20 m long and 0.8 m high with 1000 cells in the x direction and 100 cells in the z direction with the grid sizes set to $\Delta x = 0.02$ m and $\Delta z = 0.008$ m. This is similar to that of Bradford (2000), where $\Delta x = 0.02$ m and $\Delta z = 0.0075$ m are used. The kinematic viscosity is set to $v = 1.002 \times 10^{-6}$ m^2/s. For the simulation, four levels of k–l equations are solved, which gives the cut-off length scale as $l_4 = 0.0016$ m.

In this study, the simulations were conducted for 40 and 60 s of waves for the spilling and plunging breaking waves, respectively. Fig. 5 shows an example of the simulated results. It is noticed that the length of the simulation in this study is similar to that presented by Christensen et al. (2000), but significantly longer than those presented by Lin and Liu (1998a,b), 18.6 and 22.4 s for spilling and plunging breaker, respectively, and Bradford (2000) 20 and 30 s for spilling and plunging breaker, respectively. Fig. 5 shows that within the simulation time, the surface elevation, horizontal velocities, and especially the subgrid kinetic energy become almost periodic (by periodic we mean the mean value is almost steady). More importantly, it is recognized that in the present study, we did not use the damping function as that requested by Hsu et al. (2002) for their Reynolds stress model to obtain the right kinetic energy level. Through out the computations, the last five waves are used to obtain the mean value for the analysis.

5.1. Spilling breaker

For the spilling breaker case, the incident wave height is 0.125 m at the constant depth section, and the wave period is 2.0 s. Waves break on a 1/35 slope at breaking point $x_b = 6.4$ m with the breaking wave height H_b 0.163 m in the experiment.

Fig. 6 shows comparison of simulated and measured instantaneous surface elevations from the shoaling region until the bore region. The surface elevations show typical shallow water waves with shorter, higher wave crest and longer, flatter wave trough. As waves shoal, the wave crests become even more peaky with increasing wave height, with a maximum height at $x = 6.5$ m. Finally, waves reach a point where they become unstable, and then they break. Much energy has been lost at the breaking point, wave heights become smaller, and surface elevations show a kind of "saw tooth" shape with steep wavefront and long tail at the back face of the wave. In this case, the breaking event occurs between $x = 6.5$ m and $x = 7.5$ m. It can be seen that the model results agree very well with the experimental measurements.

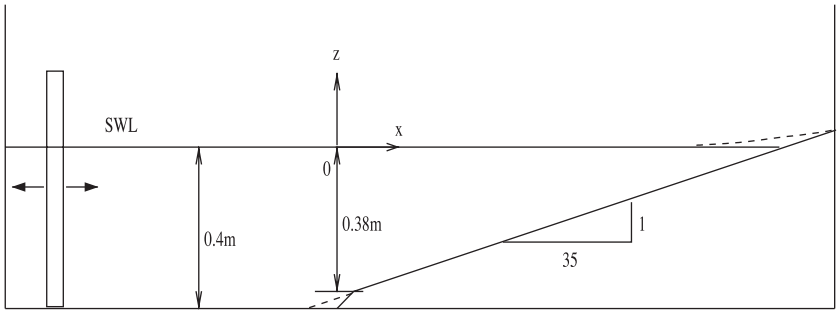

Fig. 4. Experimental set-up (Ting and Kirby, 1994).

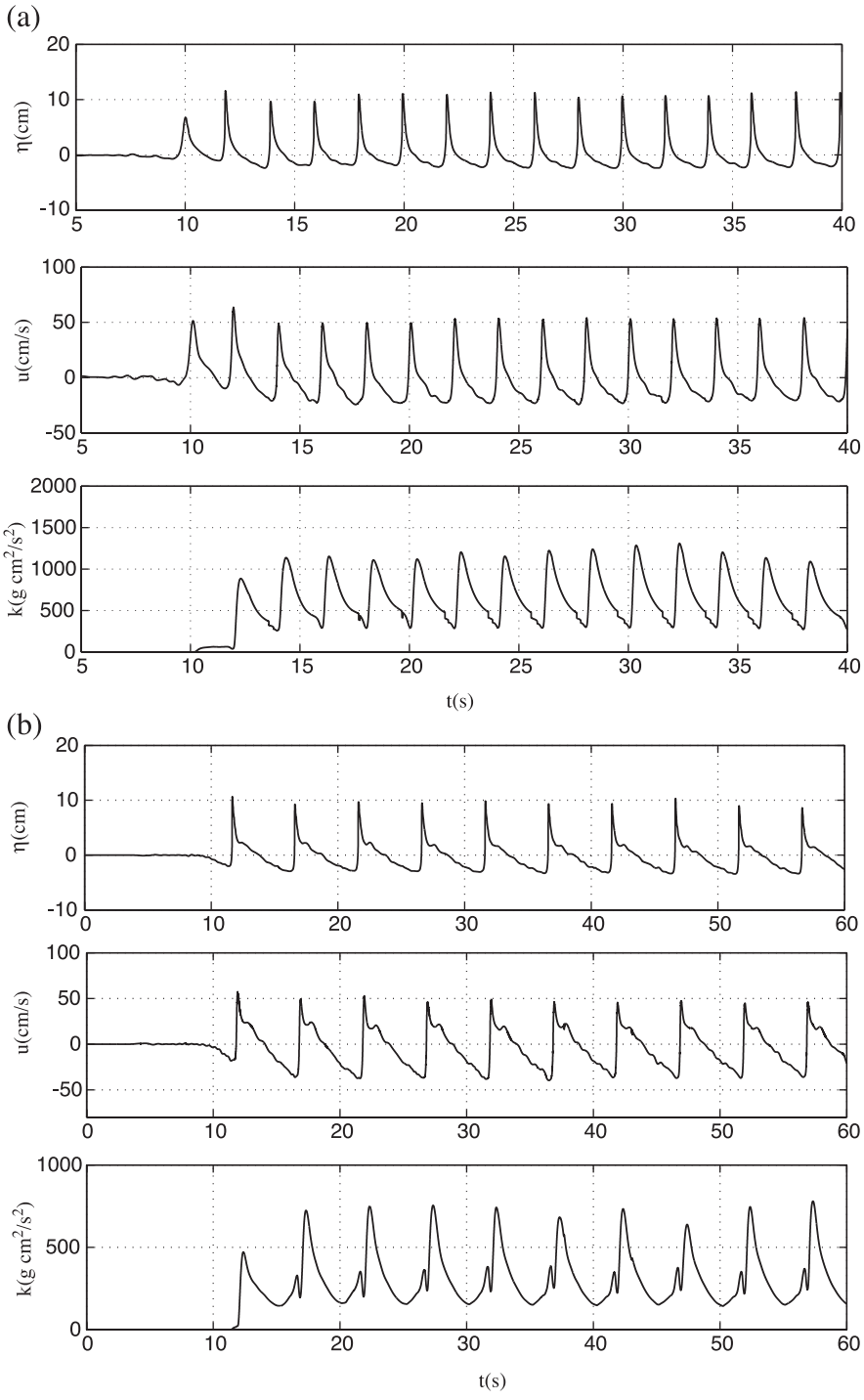

Fig. 5. Example of computed time series of surface elevation, horizontal velocities and subgrid kinetic energy. (a) Spilling breaker case. (b) Plunging breaker case. This figure shows that the subgrid kinetic energy is almost periodic in the simulation time.

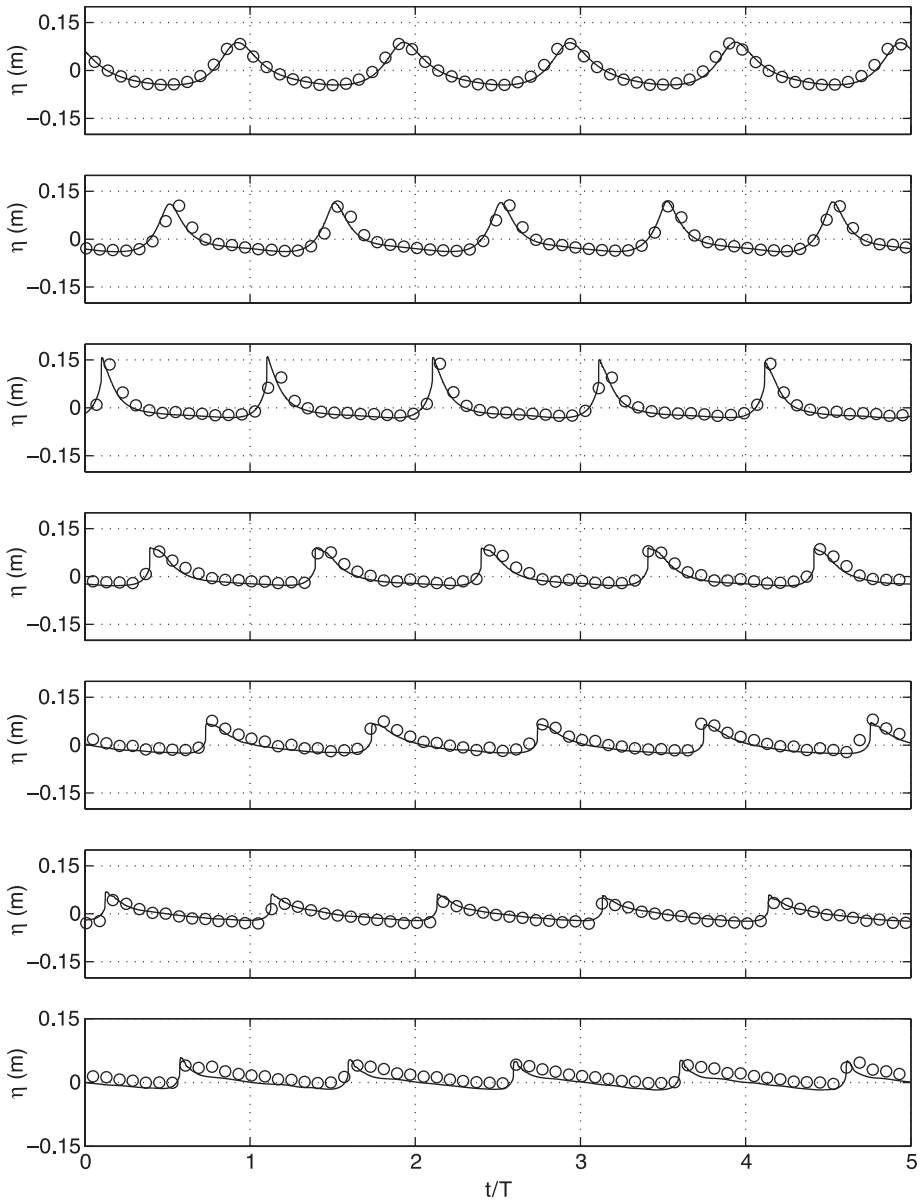

Fig. 6. Comparison of simulated (lines) and measured (circles, Ting and Kirby, 1995) instantaneous surface elevations for the spilling case. From top to bottom, at locations $x = 2.5, 4.5, 6.5, 7.5, 8.5, 9.5, 10.5$ m.

Fig. 7 presents the phase averaged surface elevations at four measured locations from nearest to the breaking point, Fig. 7(a) to the bore region, Fig. 7(d), with the experimental data shown in the left-hand column, the present model results are shown in the middle column and the results from the Reynolds stress model shown in the right-hand column. In general, the present model results agree very well with the experimental measurements but slightly overestimates the surface elevation in the inner surf zone. The Reynolds stress model, on the other hand, significantly underestimates the surface elevation near the breaking point, but with improving accuracy in the inner surf zone.

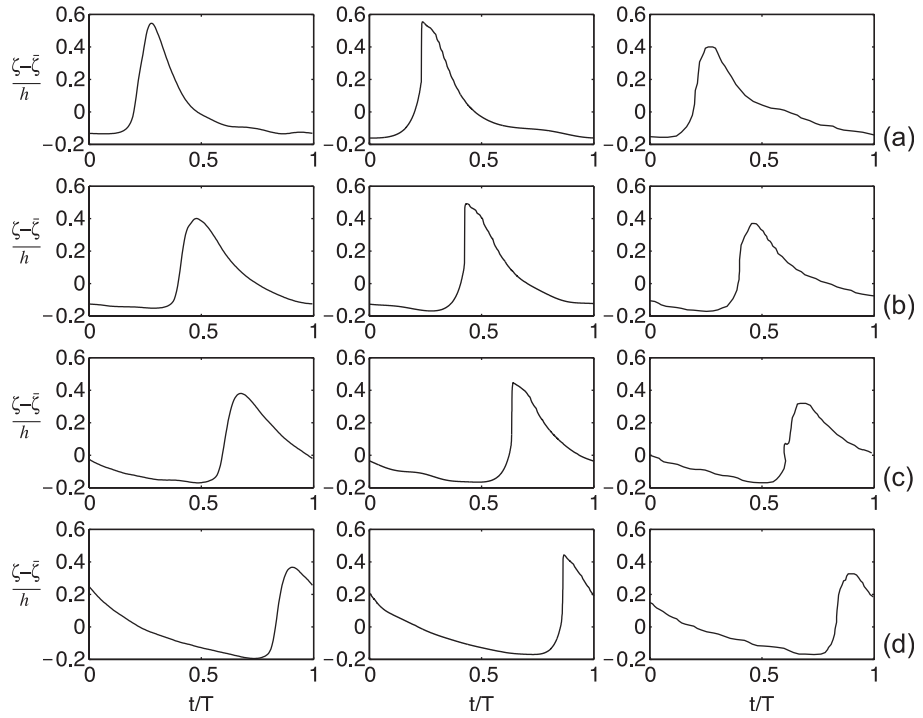

Fig. 7. Comparison of measured and simulated phase averaged surface elevations for the spilling breaker case. Left column: experimental data from Ting and Kirby (1996), middle column: results from the present model, right column: results from the Reynolds stress model (Lin and Liu, 1998a). From top to bottom (a–d) at locations $x = 7.275$, 7.885, 8.495, 9.110 m.

The computed wave crest elevations and wave trough depressions are shown in Fig. 8 where the solid lines are the results from the present simulation, the dashed lines are the RNG model results from Bradford (2000), and the circles are the experimental data of Ting and Kirby (1994). Fig. 8 shows that both models accurately simulate the wave trough, and the wave shoaling is also well predicted. The computed breaking point predicted by the present model is at $x_b = 6.16$ m, which is very close to the measured

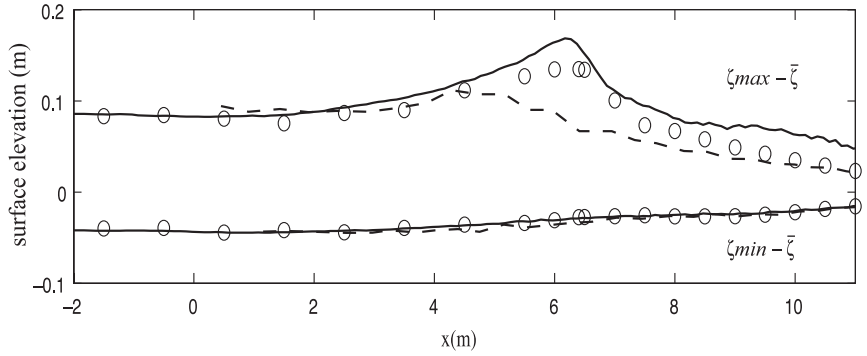

Fig. 8. Comparison of modeled and measured wave crest elevations and trough depressions of the spilling breaker case. Solid lines: present model; dashed lines: the RNG model (Bradford, 2000); circles: experimental data from Ting and Kirby (1994).

breaking point of $x_b = 6.4$ m. However, the present model slightly overestimates the wave heights near the breaking point as well as the wave heights at the inner surf zone. The RNG model, however, predicts the breaking point at around $x = 4.25$ m, which is much earlier than the experimental measurement and significantly under predicts the wave height in the outer surf zone. This result shows the same trend as

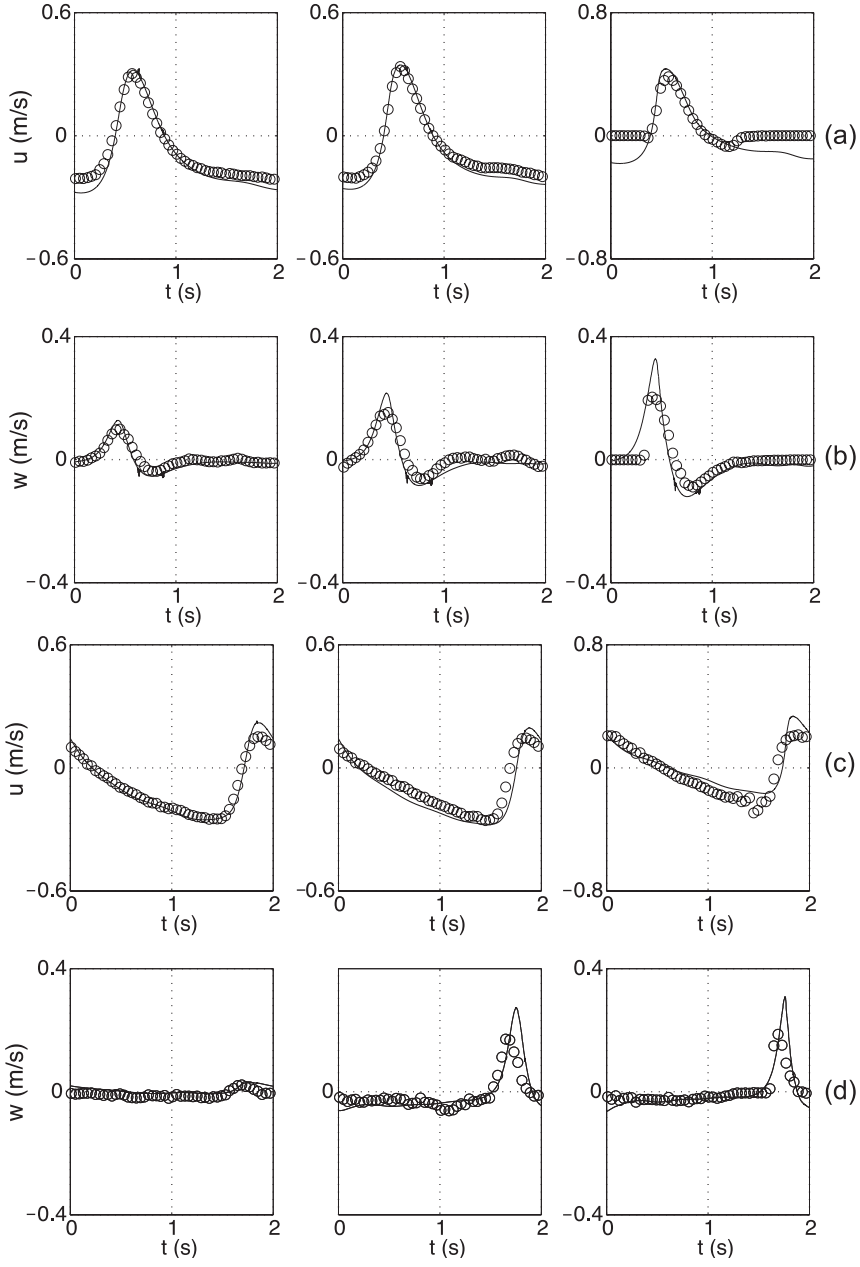

Fig. 9. Comparison of phase averaged horizontal and vertical velocities in the region of initial breaking $x = 7{:}275$ m (a, b) and in the propagating bore region $x = 9{:}110$ m (c, d) for the spilling breaker case. The vertical locations are, from left to right, $z = -0.10;\ -0.06;\ -0.02$ m. Lines: the present model; circles: experimental data from Ting and Kirby (1994).

that obtained using the $k-\epsilon$ model, k model (Fig. 1 in Bradford, 2000) and the Reynolds stress model (Lin and Liu, 1998a) as shown in Fig. 7.

The phase averaged horizontal and vertical velocities are presented in Fig. 9. The general agreement between the simulated and the experimental results is very good. However, it seems the accuracy of the numerical model is decreasing toward to the free surface. Moreover, the experiment indicates that $z=-0.02$ m is above the trough level, but in the numerical model, this point is one grid below the trough level. We expect that this is mainly due to the numerical resolution near the free surface not being high enough.

Fig. 10 shows the measured and computed undertow profiles at six measured locations. The agreement between the present model simulation and the experimental measurement is very good with the structure and magnitude well represented. The RNG model, however, seems to underestimate the undertow in general and fails to capture the vertical structure. The $k-\omega$ model presented by Christensen et al. (2000) seems to show similar trends.

5.2. Plunging breaker

For the plunging breaker case, the incident wave height is 0.128 m at the constant-depth section, and the wave period is 5.0 s. The measured breaking point is around $x_b=7.795$ m with the breaking wave height $H_b=0.163$ m.

The phase averaged surface elevations for the plunging breaker case at four measured locations are presented in Fig. 11. The experimental results are presented in the left-hand column, the present model results in the center column and the Reynolds stress model results in the right-hand column. Again, the present model shows very good agreement with the experimental data. The Reynolds stress model still underestimates the surface elevation near the breaking point, as shown in Fig. 11(a). However, comparing

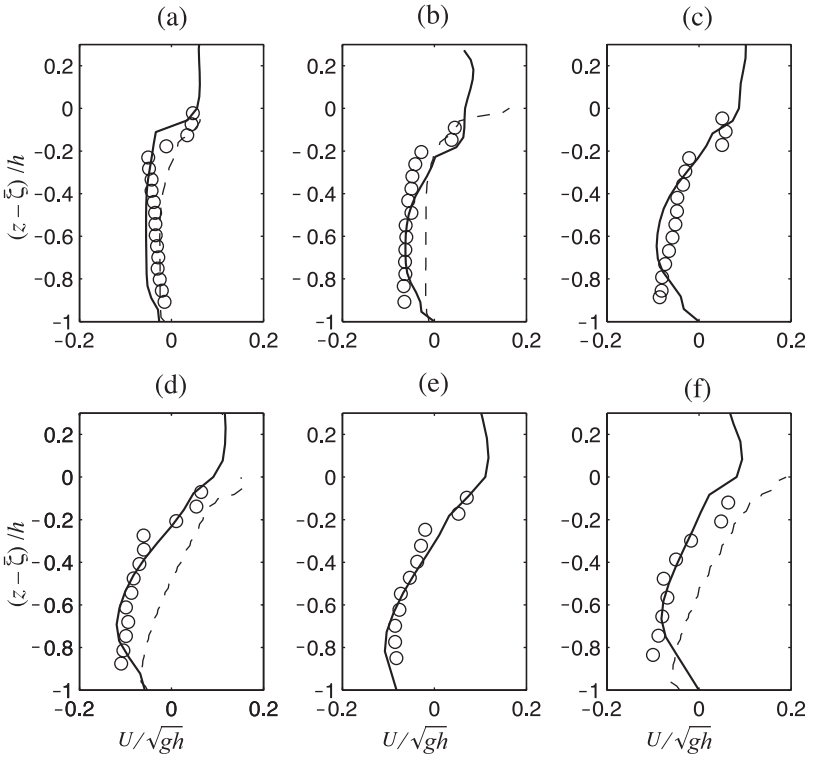

Fig. 10. Comparison of modeled and measured undertows for the spilling breaker case. Solid lines: present model; dashed lines: the RNG model (Bradford, 2000); circles: experimental data from Ting and Kirby (1994). From (a) to (f) at locations $x=6.665$; 7.275; 7.885; 8.495; 9.110; 9.725 m.

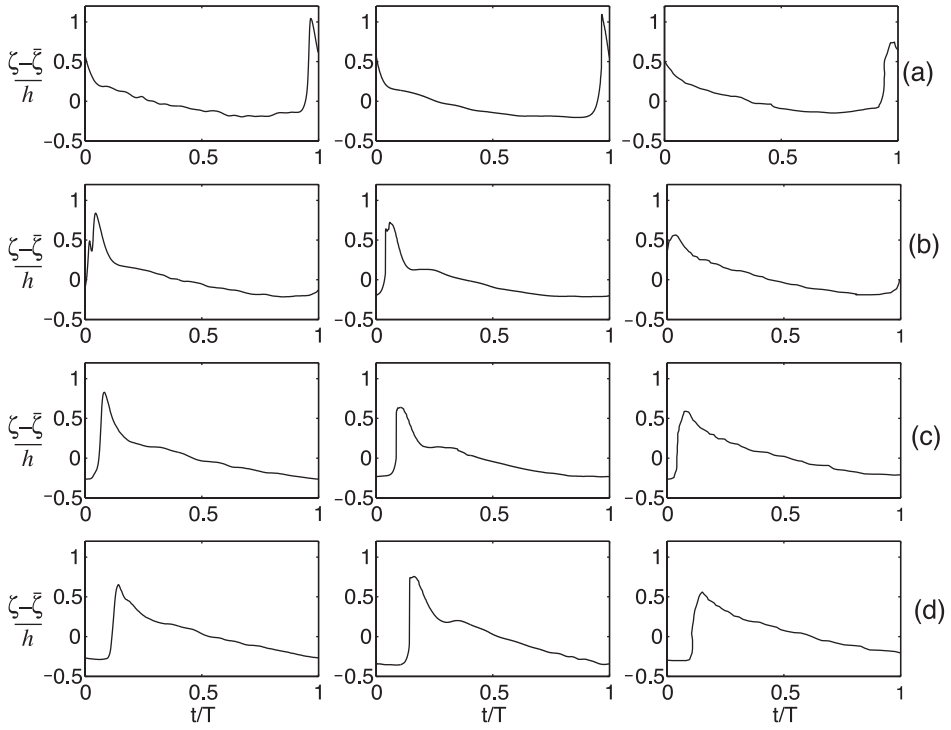

Fig. 11. Comparison of measured and simulated phase averaged surface elevations for the plunging breaker case. Left column: experimental data from Ting and Kirby (1995), middle column: results from the present model, right column: results from Reynolds stress model (Lin and Liu, 1998b). From top to bottom (a–d) at locations $x=7.795$; 8.345; 8.975; 9.295 m.

with Fig. 7, we can see that the accuracy of the Reynolds stress model seems to be improving as compared to the spilling breaker case. It is noticed that the experimental result, left column in Fig. 11(b), shows a secondary wave due the splashing of the plunging breaker. In the present model, middle column in Fig. 11(b), this secondary wave is predicted, but smaller than the experimental, while in the Reynolds stress model, this secondary wave is completely missing.

The comparison of wave crest elevations and wave trough depressions is presented in Fig. 12. It is seen

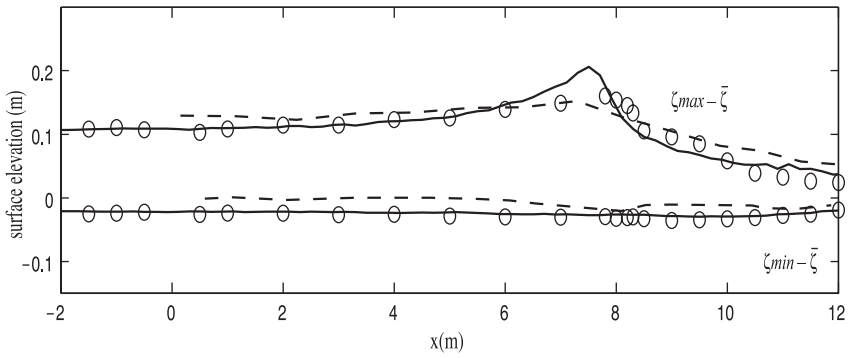

Fig. 12. Comparison of modeled and measured wave crest elevations and trough depressions for the plunging breaker case. Solid lines: present model; dashed lines: the RNG model (Bradford, 2000); circles: experimental data from Ting and Kirby (1994).

that the wave trough is very accurately predicted by the present model, as well as the wave crest in the shoaling and the bore region. However, the present model overestimates the wave crest near the breaking point, while the RNG overestimates the wave trough in general and underestimates the wave crest. Comparing with Fig. 8, it is seen that the RNG model does a better job in predicting wave crest distribution in the

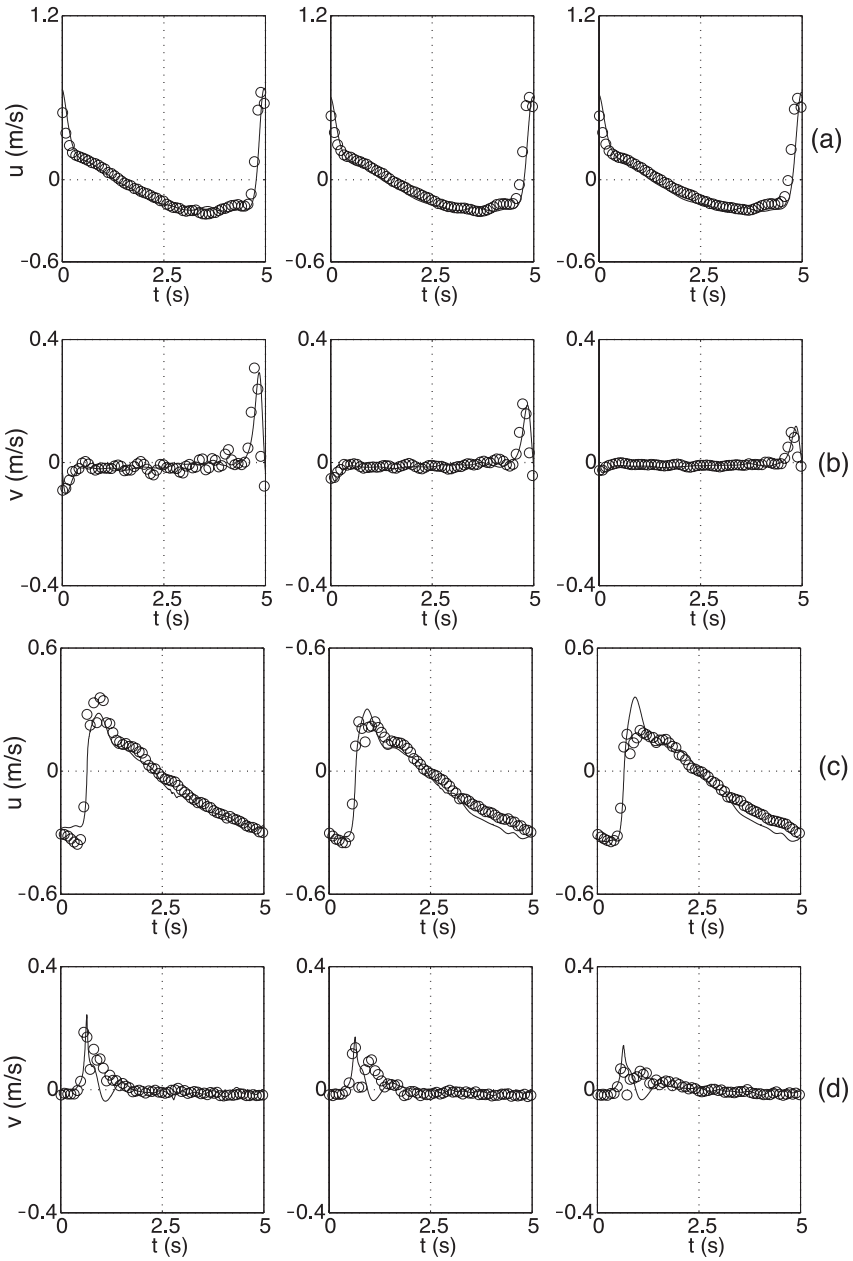

Fig. 13. Comparison of phase averaged horizontal and vertical velocities for the plunging breaker case. In the region of initial breaking, $x=7.795$ m (a, b) at $z=-0.115$; -0.08; -0.04 m from left to right, and in the propagating bore region $x=9.295$ m (c, d) at $z=-0.08$; -0.06; -0.04 m from left to right. Lines (present model), circles: experimental data from Ting and Kirby (1995).

plunging breaker case than in the spilling breaker case, consistent with the Reynolds stress model results as shown in Fig. 11.

Fig. 13 shows the simulated and measured phase averaged horizontal and vertical velocities. The computational results were obtained from the last five waves in the simulation. The upper two panels are the horizontal (a) and vertical (b) velocities at the breaking point $x = 7.795$ m, while the lower panels (c, d) are the results in the inner surf zone at $x = 9.295$ m. The agreement between the numerical simulation and the experimental results is generally good. The discrepancies that exist are mainly in the vertical velocity (d) at $x = 9.295$ m, where the experiment shows a strong secondary wave motion due to the splashing of the primary wave which the numerical model failed to capture. Although our model is capable of simulating a large overturning free surface (see Appendix A), obtaining the fine detail for a strong overturning is computationally difficult, as noted by Lin and Liu (1998b) and Bradford (2000). Lin and Liu (1998b) observed that in spite of this difficulty with the fine detail the mean flow mechanism is correctly captured with simulations of this type.

The undertow profiles of the plunging breaker case are presented in Fig. 14. The agreement between the measured data and the present model prediction is reasonably good, showing that the present model can predict the undertow accurately in the outer surf zone. The general agreement of the undertow in the inner surf zone is also good, except that the numerical model shows slightly more curvature than the experimental measurements. The data seem to show stronger mixing than the model results, we think that the air bubbles in the physical experiments may have contributed some of this

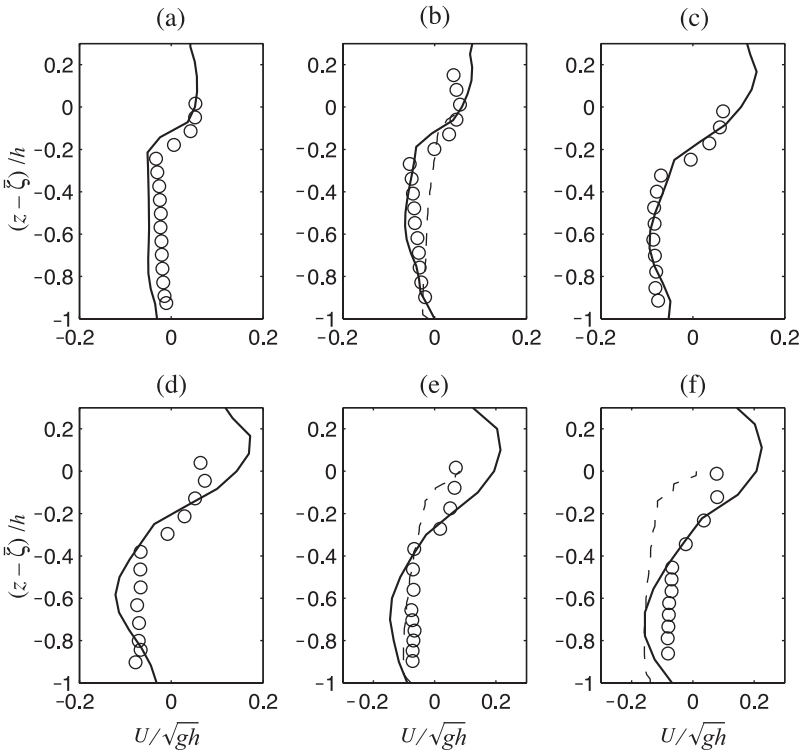

Fig. 14. Comparison of modeled and measured undertows for the plunging breaker case. Solid lines: present model; dashed lines: the RNG model (Bradford, 2000); circles: experimental data from Ting and Kirby (1994). From (a) to (f) at locations $x = 7.795$; 8.345; 8.795; 9.295; 9.795; 10.395 m.

mixing. This effect, however, is not accounted in the numerical model yet. The RNG model seems to do a fairly good job in the outer surf zone but overestimates the undertow at the inner bore region.

6. SGS turbulent transport mechanism

In this section, we will provide some discussion of the SGS turbulent transport mechanism using the present model. Some of the questions we are interested in are: Where are the horizontal vortices formed in a breaking wave? Where does turbulent production and dissipation take place? Does the turbulent production and dissipation reach an equilibrium? What's the contribution of turbulent convection and diffusion to the turbulent kinetic energy transport?

First we will look at the horizontal vorticity, $\omega=(\partial u)/(\partial z)-(\partial w)/\partial x$, for the spilling and the plunging breaker case, shown in Figs. 15 and 16, respectively[1]. In Fig. 15, it is shown that the vorticity generated by the breaking waves is initiated at the toe of the wavefront right before the breaking point, this vortex is further strengthened and convected to almost the whole crest region. We also found that there is substantial vorticity generated at the solid boundary associated with the wave crest. This vorticity, as indicated by the computation, is due to the angle between the horizontal bottom and the sloping beach. The vorticity structure shown here is very similar to that found using a algebra Reynolds stress model (Lin and Liu, 1998a). However, with that model, the vorticity appeared about 2.40 m before the measured breaking point, with the present model the vorticity appears right before the breaking point, which seems to be more reasonable. Fig. 16 presents the simulated horizontal vorticity for the plunging breaker case. Comparing with the results from the spilling breaker, we see that the horizontal vorticity in the plunging breaker case is stronger and covers a larger region of the water body.

The snap shots of SGS turbulent kinetic energy are presented in Fig. 17 for the spilling case and Fig. 18 for the plunging breaker case. Fig. 17 shows that the turbulent kinetic energy is generated just before the breaking point and is higher in the upper region and forward face of the wave. The turbulent kinetic energy is convected and diffused to the back face of the wave, with a considerable amount remaining behind as the wave moves into the surf zone. Fig. 18 shows that under the plunging breaker, the SGS turbulent kinetic energy is dissipated much faster than under the spilling breaker. Almost all of the turbulent kinetic energy is dissipated within one wave period under the plunging breaker.

The SGS turbulent production is shown in Figs. 19 and 20, for the spilling and plunging breaker case, respectively. Figs. 19 and 20 show that the SGS turbulent production takes place above the wave trough and at the wavefront, initiated right before the breaking point. As waves approach the shoreline, the turbulent production extends to appear in the whole crest region continuing into surf zone.

The SGS turbulent dissipation is presented in Figs. 21 and 22, for the spilling and plunging breaker case, respectively. Both figures show that the SGS turbulent dissipation appears at about the same time as the turbulent production, but is localized mainly at the back face of a wave, with no turbulent dissipation directly under the wave crest. As the wave approaches the shore, the turbulent dissipation forms a long tail at the back face of the wave for the spilling breaker case. The SGS turbulent dissipation is more localized under the plunging breaker. This means that most of the turbulent kinetic energy is rapidly dissipated within one wave period for the plunging breaker. It is seen from Figs. 19–22 that in both cases, the SGS turbulent production and turbulent dissipation are of the same order.

In order to understand the SGS production and dissipation more clearly, we present results showing regions where the SGS turbulent production is stronger than turbulent dissipation in Figs. 23 and 24 and the opposite in Figs. 25 and 26, for the spilling and plunging breaker case, respectively. These figures illustrate that the SGS turbulent production is dominant at the initial stage of the breaking wave and at the front face of a wave. The SGS turbulent dissipation is dominant at the back face of a wave. For the spilling breaker case, there is significant amount of turbulent kinetic energy being dissipated in the inner surf zone, while for the plunging breaker case, most turbulent

[1] To see the color figures in this section go to the online version of this paper, or contact the authors.

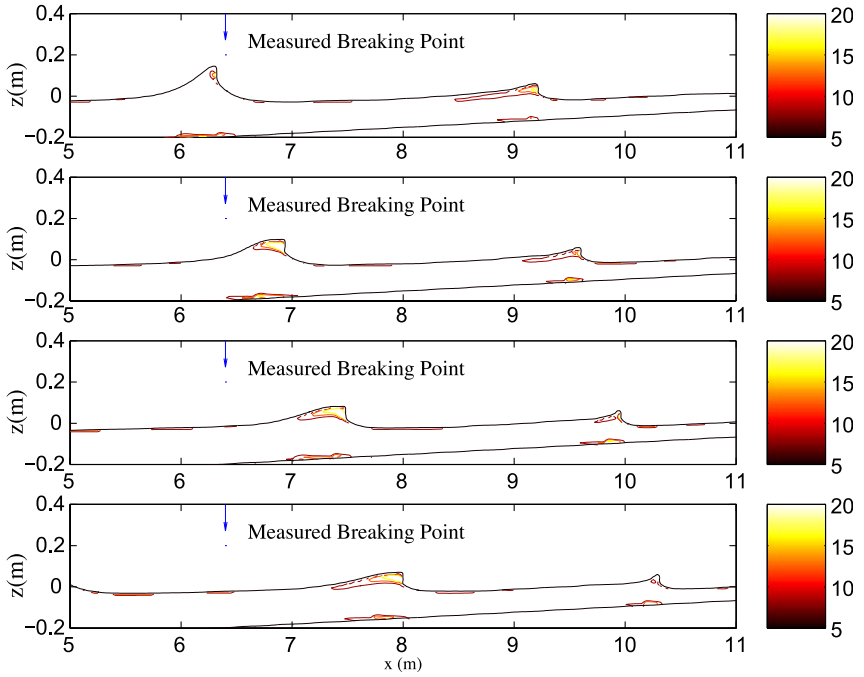

Fig. 15. Simulated horizontal vorticity of the spilling breaker case. Unit: 1/s.

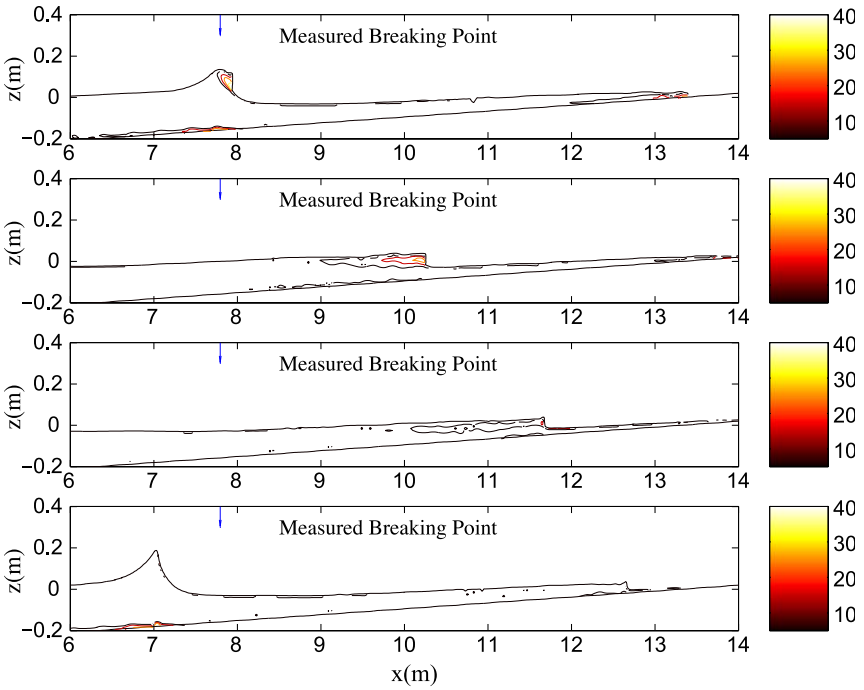

Fig. 16. Simulated horizontal vorticity of the plunging breaker case. Unit: 1/s.

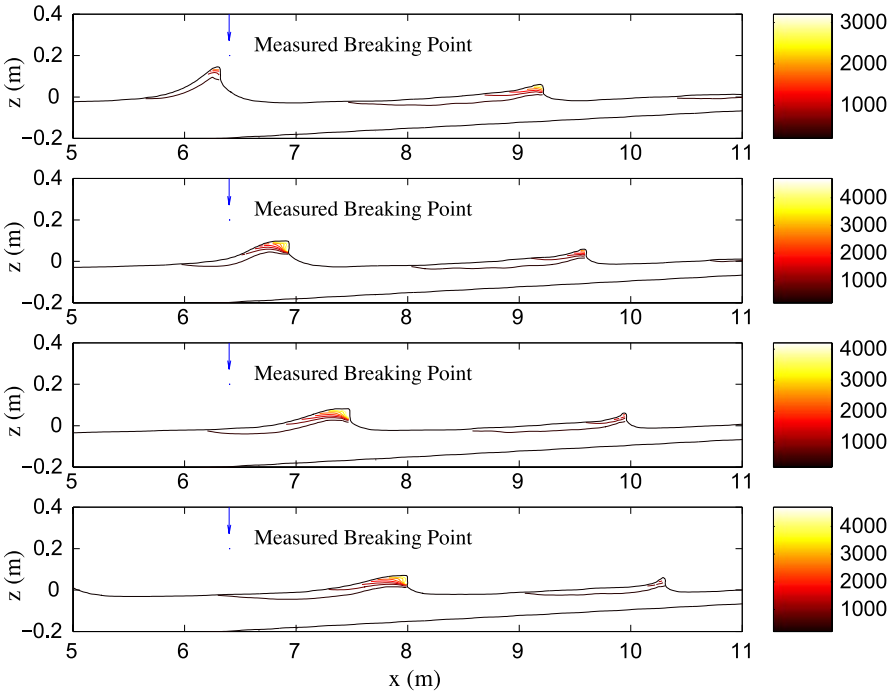

Fig. 17. Simulated SGS turbulent kinetic energy of the spilling breaker case.

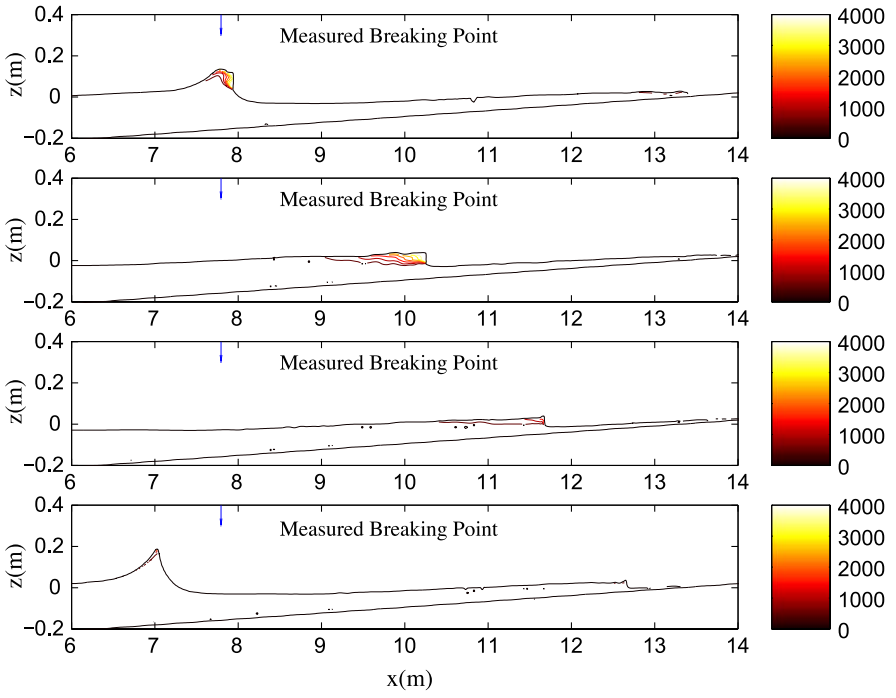

Fig. 18. Simulated SGS turbulent kinetic energy of the plunging breaker case.

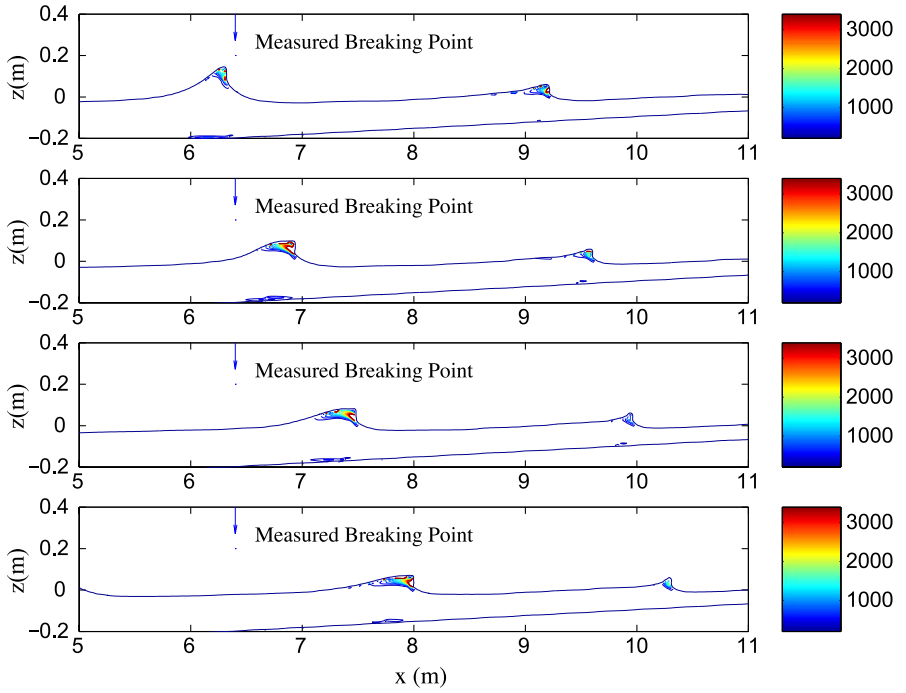

Fig. 19. Simulated SGS turbulent production of the spilling breaker case.

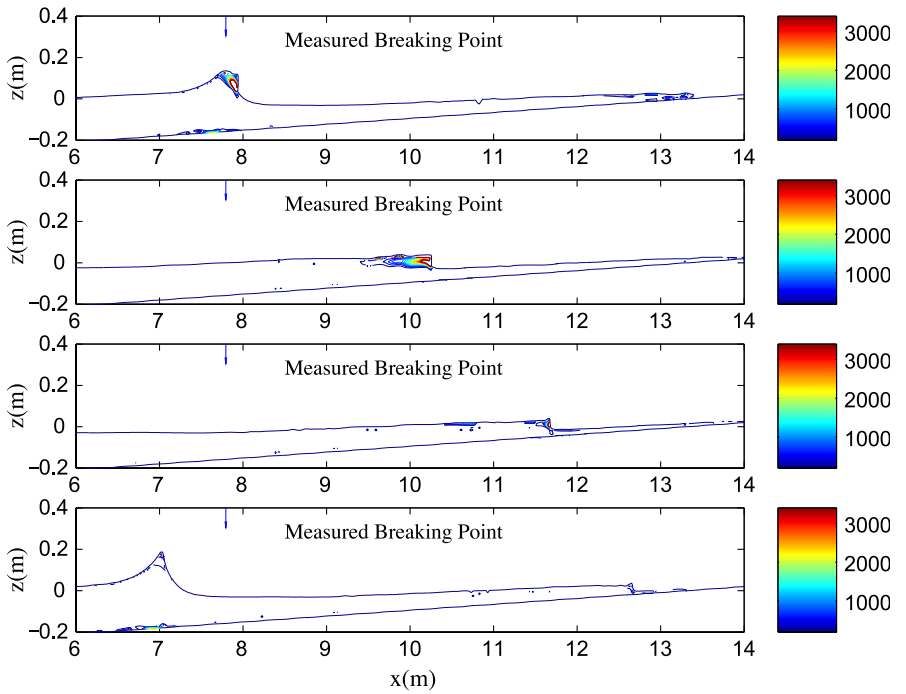

Fig. 20. Simulated SGS turbulent production of the plunging breaker case.

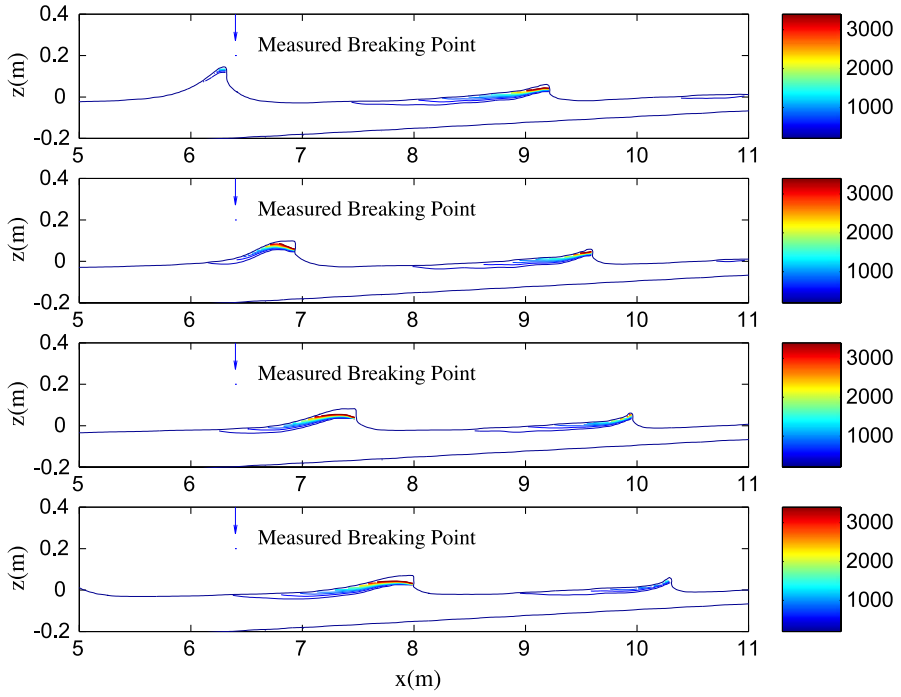

Fig. 21. Snap shot of SGS turbulent dissipation of the spilling breaker case. Notice that there is no dissipation directly under the wave crest.

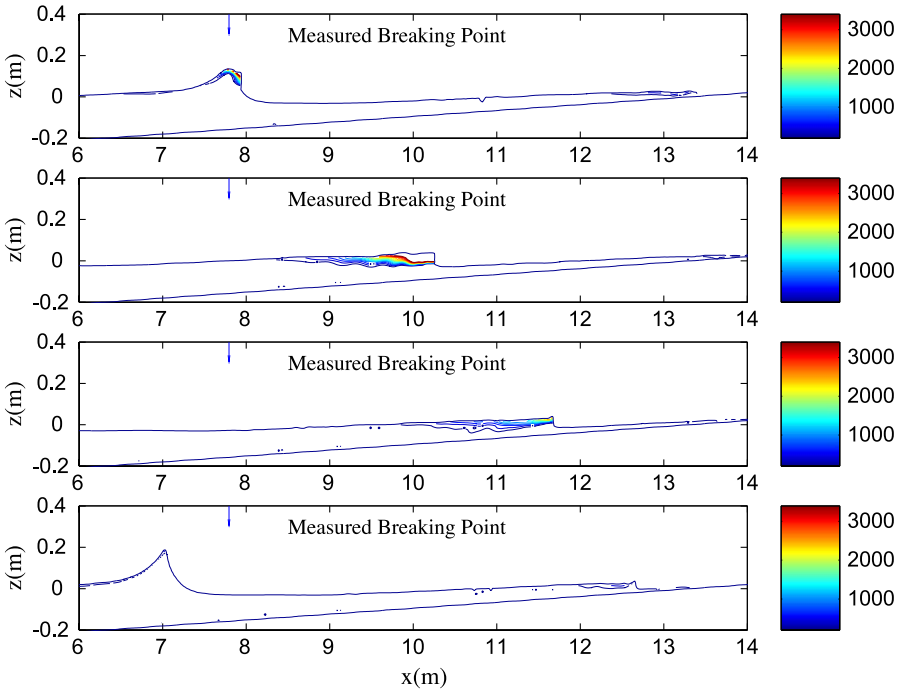

Fig. 22. Snap shot of SGS turbulent dissipation of the plunging breaker case. Notice that there is no dissipation directly under the wave crest.

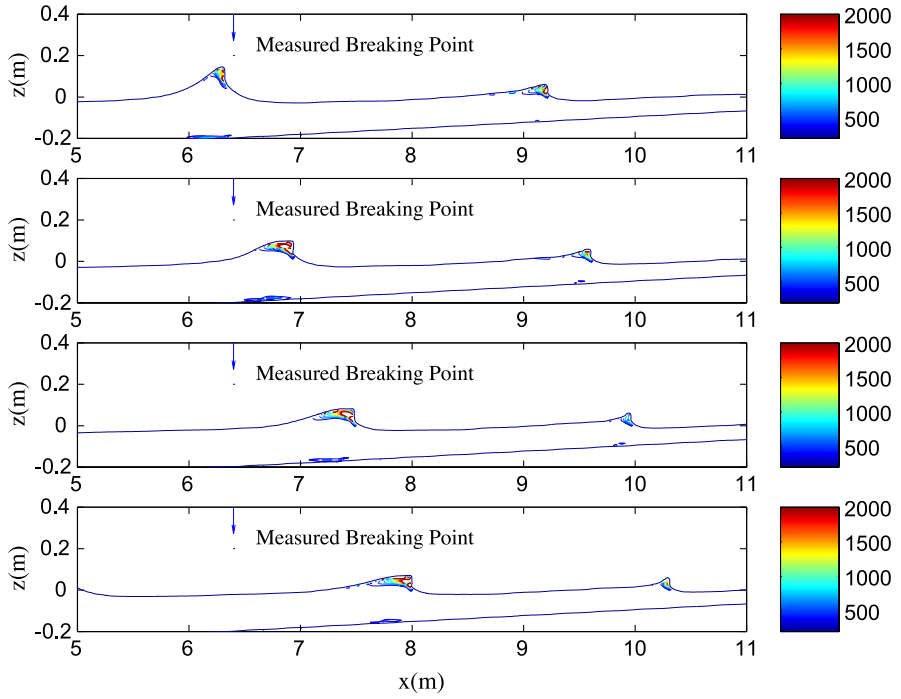

Fig. 23. Contour plot of SGS turbulent production >SGS turbulent dissipation (PROD $-\epsilon>0$) of the spilling breaker case.

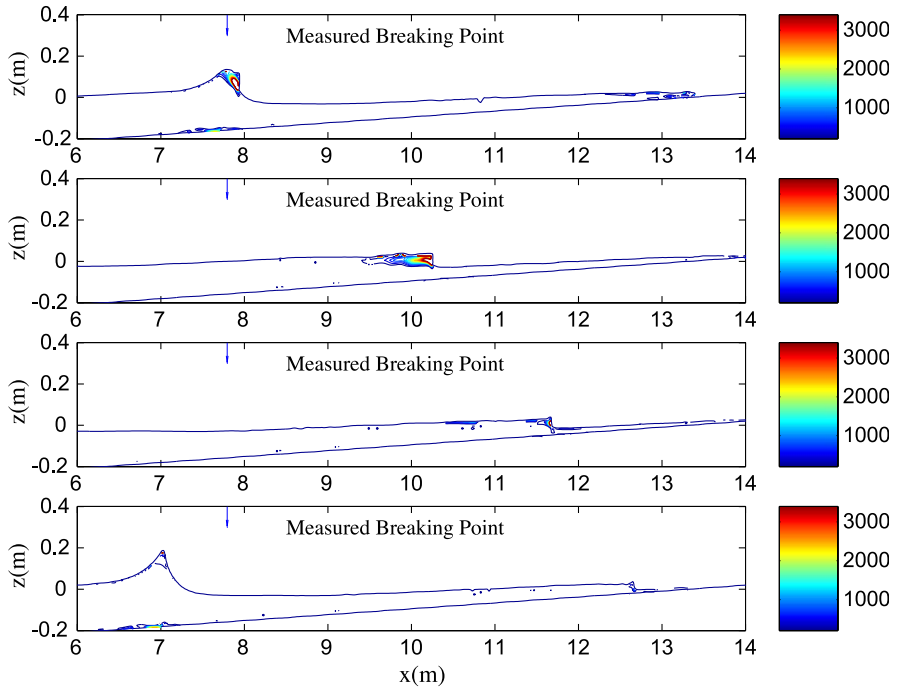

Fig. 24. Contour plot of SGS turbulent production >SGS turbulent dissipation (PROD $-\epsilon>0$) of the plunging breaker case.

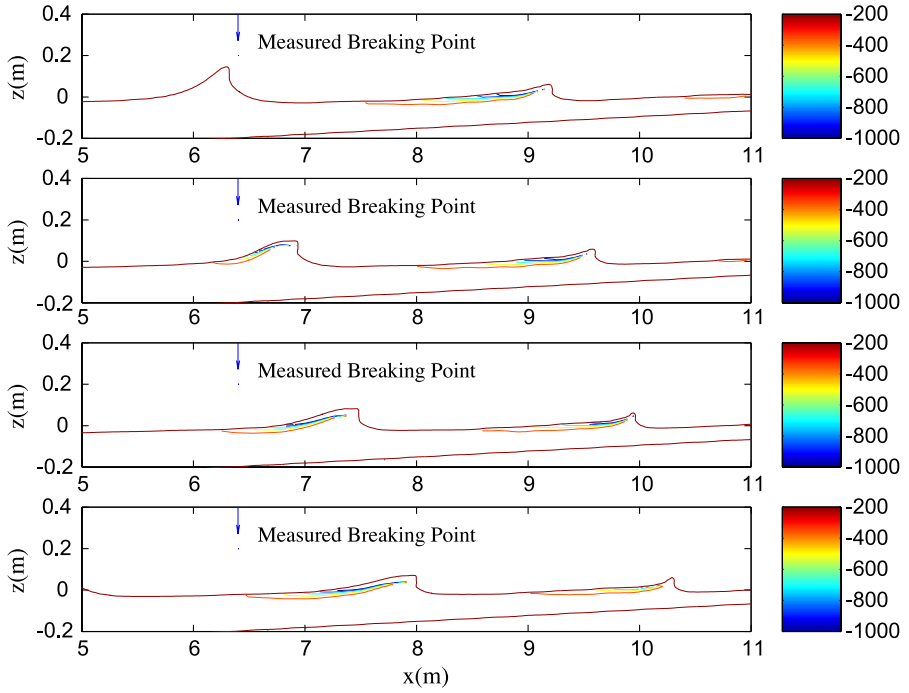

Fig. 25. Contour plot of SGS turbulent production $<$SGS turbulent dissipation (PROD $-\epsilon<0$) of the spilling breaker case.

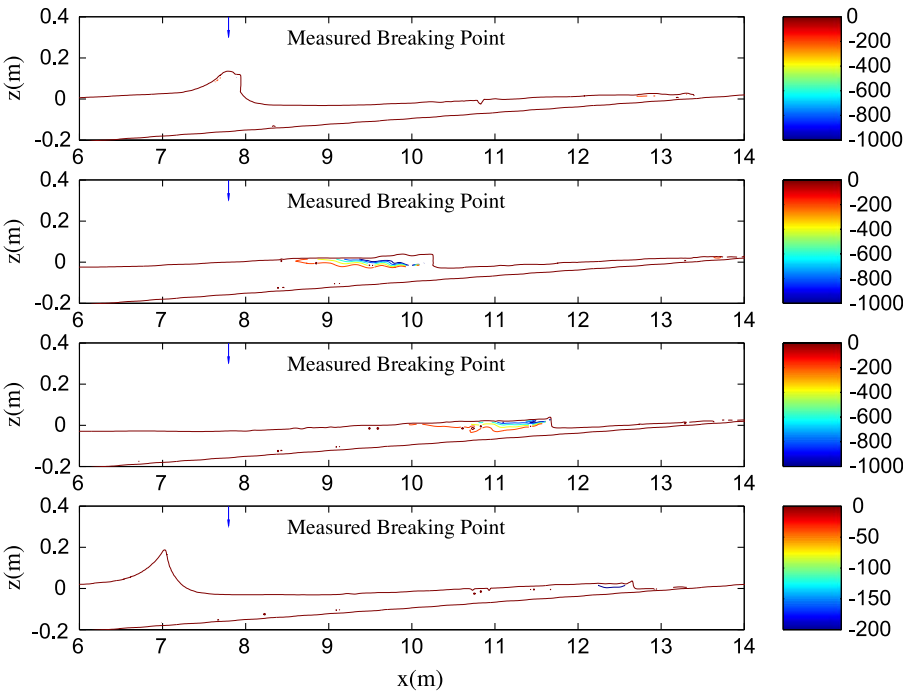

Fig. 26. Contour plot of SGS turbulent production $<$SGS turbulent dissipation (PROD $-\epsilon<0$) of the plunging breaker case.

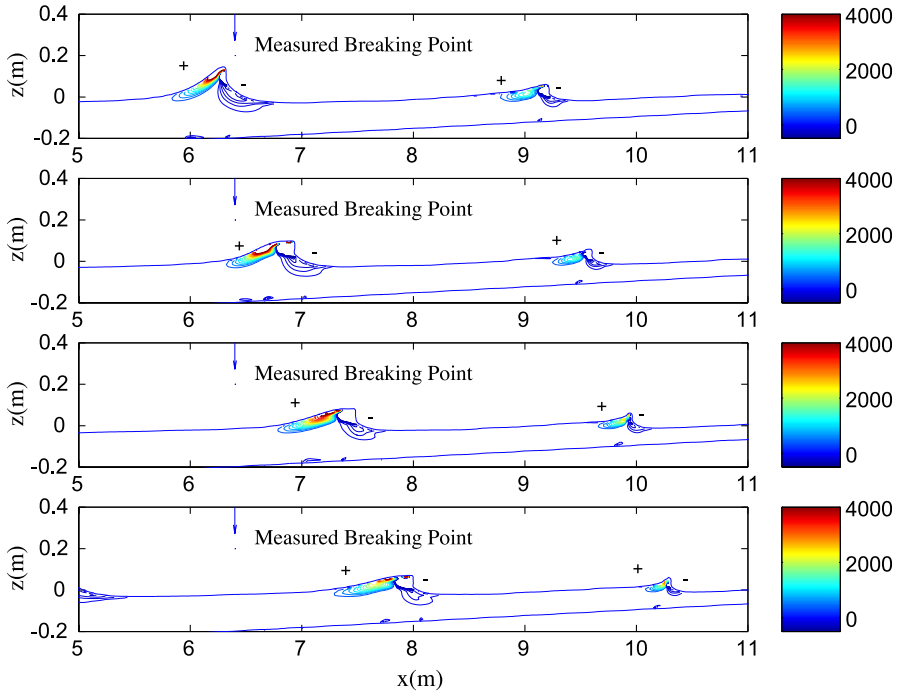

Fig. 27. Snap shot of SGS turbulent convection of the spilling breaker case.

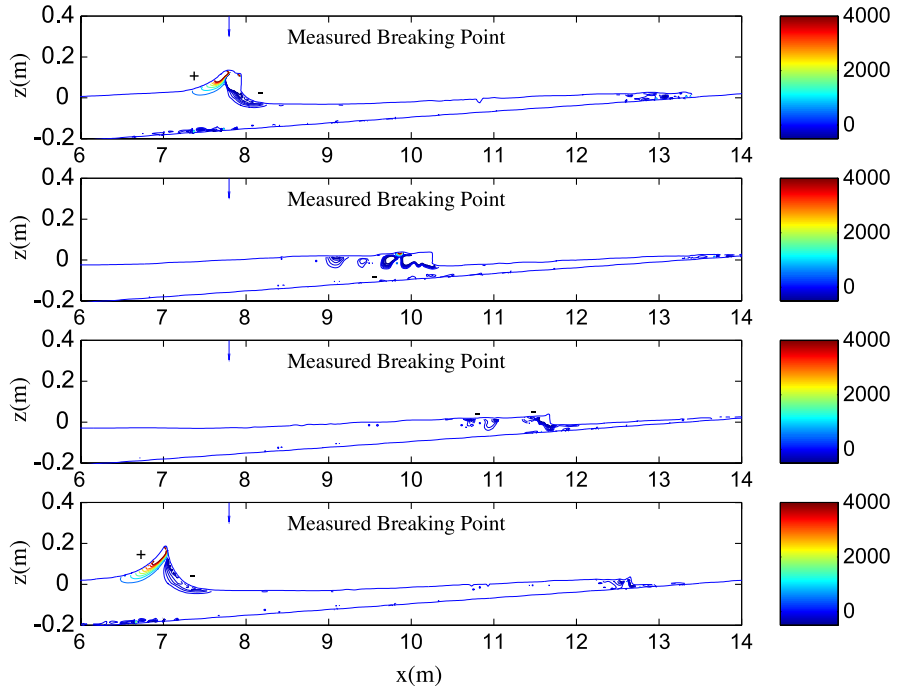

Fig. 28. Snap shot of SGS turbulent convection of the plunging breaker case.

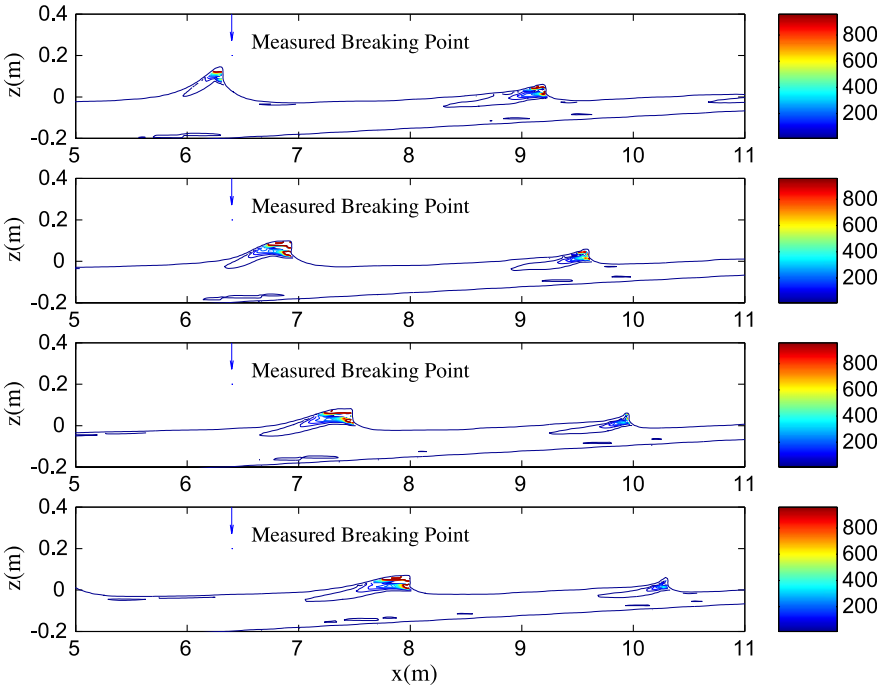

Fig. 29. Snap shot of SGS turbulent diffusion of the spilling breaker case.

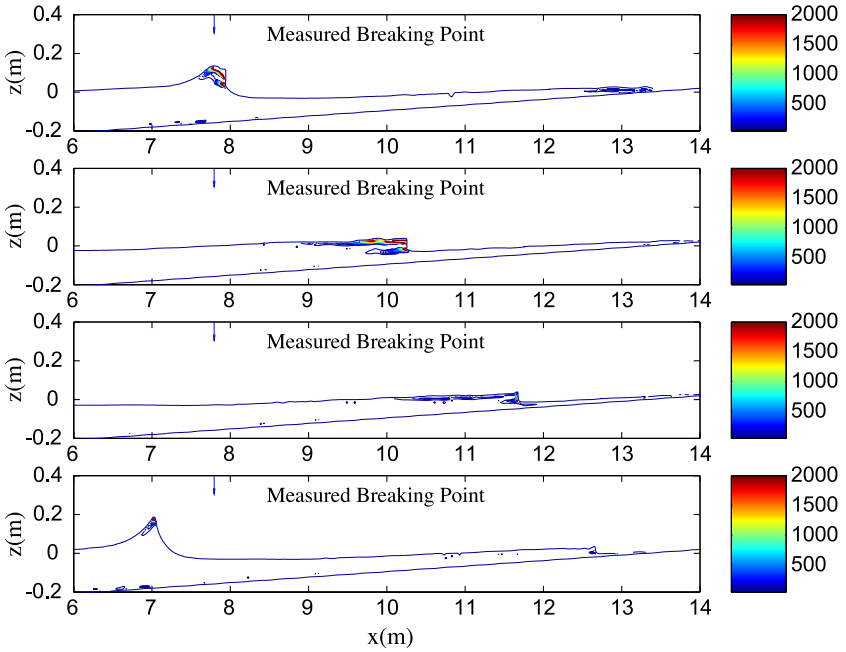

Fig. 30. Snap shot of SGS turbulent diffusion of the plunging breaker case.

kinetic energy is dissipated within one wave period. The equilibrium assumption of turbulent production and dissipation seems to be less satisfied for the spilling breaker case. Therefore, we conclude that the turbulent production and dissipation being in equilibrium are only a good approximation for both spilling and plunging breakers below the trough level. At the inner surf zone, this assumption is good for the plunging breaker case alone.

Results showing SGS turbulent convection are shown in Figs. 27 and 28 for the spilling and plunging breaker, respectively. The convective terms are defined as $-\vec{V}\cdot\nabla k$. The computation shows the vertical convection plays a more important role than the horizontal convection above the wave trough, i.e., $-w(\partial k)/(\partial y) \gg -u(\partial k)/(\partial x)$. Figs. 27 and 28 show that the convection terms increase the turbulent kinetic energy at the back face of the wave (the kinetic energy is transported downward (+) (because $(\partial k)/(\partial y)>0$, therefore, we have $w<0$), but decrease the kinetic energy at the front face of the wave below the trough level ($-$) (the kinetic energy is transported upward). Comparing the spilling breaker and the plunging breaker, Figs. 27 and 28, respectively, we also see that under the plunging breaker, the downward transport of turbulent kinetic energy finished rapidly, i.e., the turbulent kinetic energy is being convected downward much faster than that under the spilling breaker.

Figs. 29 and 30 show the SGS diffusion terms for the spilling and plunging breaker, respectively. Comparing with the convective terms (Figs. 27 and 28), we see that turbulent convection and diffusion are of the same order at the trough level, above the trough level, however, turbulent convection dominates. Therefore, neglecting the convection terms in the turbulent closure model will most likely introduce errors above the wave trough.

7. Conclusions

A two-dimensional multi-scale turbulence model based on VOF method is proposed to simulate breaking waves. The numerical model has been tested with experimental measurements as well as other RANS model results, namely Reynolds stress model and RNG model, under spilling and plunging breaking waves. In general, the present model showed favorable agreements to the experimental measurements over RANS type model results in terms of surface elevations, particle velocities, wave height distributions and undertow profiles. The improvement is especially significant under the spilling breaker, when the RANS models have great difficulty in predicting surface elevations near the breaking point. While the agreement between the present model simulation and experimental data is consistent, the accuracy of the RANS model results improves under the plunging breaker. This is likely due to the fact that under the plunging breaker, the flow is closer to a spectral equilibrium where single-scale hypothesis maybe adequate.

Detailed analysis of the numerical results also showed that the SGS turbulent production mainly takes place above the trough level. Although the order of turbulent dissipation is the same as that of turbulent production, turbulent production is primarily located at the wavefront and above the wave trough, whereas turbulent dissipation is primarily located at the back face of a wave, indicating that in these regions, the assumption of local equilibrium is not correct. Below the trough level, the local equilibrium assumption is reasonable. The convection of turbulent energy by the mean flow plays an important role above the wave trough. The kinetic energy is convected upward under the wavefront and downward under the back face of a wave. The rate of upward convection is smaller than the downward convection. Turbulent convection and diffusion are of the same order at the trough level. Under the spilling breaking wave, the turbulent kinetic energy is continue to dissipate in the bore region, whereas under the plunging breaking wave, the turbulent kinetic energy is dissipated very rapidly within one wave period.

It is noticed that in all models presented here, Lin and Liu (1998b), Bradford (2000) and the present model, the air entrainment is not accounted and further improvements including the model of air are necessary.

Acknowledgements

The authors wish to thank Drs. Francis Ting and James Kirby for sending us the experimental data. Dr.

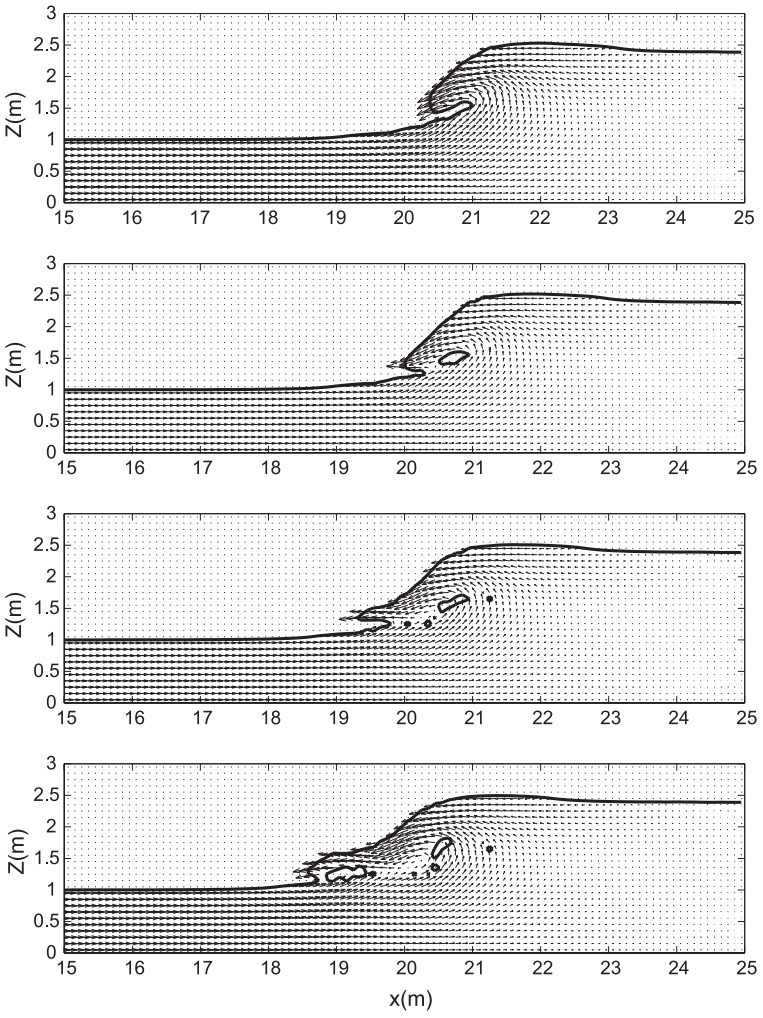

Fig. 31. An undular bore showing overturning surface simulated by the VOF model. It is noted that the present numerical model does not account for the entrainment air at this stage.

Scott Bradford for providing his RNG model results and Dr. Pengzhi Lin for providing his Reynolds stress model results. Comments from Drs. James Kirby, Ib A. Svendsen and two anonymous reviewers are gratefully acknowledged.

Appendix A. A strong plunging

Fig. 31 shows a strong plunging simulated by the VOF model. The plunging of the water surface was obtained by pushing a bulk of water to a vertical wall. It is noticed that the air is trapped inside the fluid, because the air was not modeled. Future study to take into the account of air entrainment is underway and will be reported separately.

References

Arai, M., Paul, U.K., Cheng, L.Y., Inoue, Y., 1993. A technique for open boundary treatment innumerical wave tanks. Journal of Society of Naval Architects in Japan 173, 45–50.

Bradford, S.F., 2000. Numerical simulation of surf zone dynamics. Journal of Waterway, Port, Coastal and Ocean Engineering 126 (1), 1–13.

Christensen, E.D., Deigaard, R., 2001. Large eddy simulation of breaking waves. Coastal Engineering 42, 53–86.

Christensen, E.D., Jensen, J.H., Mayer, S., 2000. Sediment transport under breaking waves. Proc. 27th Int. Conf. on Coastal Eng. ASCE, Sydney, Australia, pp. 2467–2480.

Deardorff, J.W., 1970. Numerical study of three dimensional turbulent channel flow at large Reynold numbers. J. Fluid Mech. 4, 453–480.

Guo, Z., Rhode, D.L., 1996. Assessment of two- and three-scale k–ϵ models for rotating cavity flows. Transactions of the ASME 118, 826–834.

Hanjalic, K., Launder, B.E., Schiestel, R., 1980. Multiple-time-scale concepts in turbulent transport modeling. In: Bradbury, L.J.S., et al. (Ed.), Turbulent Shear Flows, vol. 2. Springer-Verlag, New York, pp. 36–49.

Hirt, C.W., Nichols, B.D., 1981. Volume of fluid (VOF) method for dynamics of free boundaries. Journal of Computational Physics 39, 201–225.

Horikawa, K., 1988. Nearshore Dynamics and Coastal Processes: Theory, Measurement and Prediction Models. University of Tokyo Press, Tokyo, Japan. 500 pp.

Hsu, T.J., Sakakiyama, T., Liu, P.L.-F., 2002. A numerical model for wave motions and turbulence flows in front of a composite breakwater. Coastal Engineering 46 (1), 25–50.

Kawamura, T., Kawahara, K., 1984. Computation of high Reynolds number flow around a circular cylinder with surface roughness. AIAA Paper, 84–134.

Kim, S.-W., 1991. Calculation of divergent channel flows with a multiple-time-scale turbulence model. AIAA Journal 29 (4), 547–554.

Kraichnan, R.H., 1967. Inertial ranges in two-dimensional turbulence. The Physics of Fluids. 10, vol. 7, 1417–1423.

Lemos, C.M., 1992. A simple numerical technique for turbulent flows with free surfaces. International Journal of Numerical Methods in Fluids 15, 127–146.

Lilly, D.K., 1969. Numerical simulation of two-dimensional turbulence. The Physics of Fluids Supplement II, 240–249.

Lin, P.Z., Liu, P.L.-F., 1998a. A numerical study of breaking waves in the surf zone. Journal of Fluid Mechanics 359, 239–264.

Lin, P.Z., Liu, P.L.-F., 1998b. Turbulence transport, vorticity dynamics, and solute mixing under plunging breaking waves in surf zone. Journal of Geophysical Research 103, 15677–15694.

Lin, P.A., Liu, P.L.-F., 1999. Runup and rundown of solitary waves on sloping beaches. Journal of Waterway, Port, Coastal and Ocean Engineering 125 (3), 247–255.

Miyata, H., 1986. Finite-difference simulation of breaking waves. Journal of Computational Physics 65, 179–214.

Petit, H.A.H, van Gent, M.R.A., van den Boscj, P., 1994. Numerical simulation and validation of plunging breakers using a 2D Navier-Stokes model. Proc. 24th Int. Conf. on Coastal Eng. ASCE, Kobe, Japan, pp. 511–524.

Rodi, W., 1980. Turbulence models and their application in hydraulics. IAHR Monograph Series. Delft Hydraulics, Delft, The Netherlands.

Ting, F.C.K., Kirby, J.T., 1994. Observation of undertow and turbulence in a laboratory surf zone. Coastal Engineering 24, 51–80.

Ting, F.C.K., Kirby, J.T., 1995. Dynamics of surf-zone turbulence in a strong plunging breaker. Coastal Engineering 24, 177–204.

Ting, F.C.K., Kirby, J.T., 1996. Dynamics of surf-zone turbulence in a spilling breaker. Coastal Engineering 27, 131–160.

Torrey, M., Cloutman, L.D., Mjolsness, R.C., Hirt, C.W., 1985. NASA-VOF2D: a computer program for incompressible flows with free surface. Los Alamos Scientific Laboratory Report LA-10612.

Wijayaratna, N., Okayasu, A., 2000. DNS of wave transformation, breaking and run-up on sloping beds. Proc. 4th Int. Conf. on Hydrodynamics, vol. 2. IAHR, Yokohama, Japan, pp. 527–532.

Zhao, Q., 1998. Wave kinematics on a submerged reef with a steep seaward face. PhD thesis, Saitama University, Japan.

Zhao, Q., Tanimoto, K., 1998. Numerical simulation of breaking waves by large eddy simulation and VOF method. Proc. 26th Int. Conf. on Coastal Eng. ASCE, Copenhagen, Denmark, pp. 892–905.